NUCLEAR ENERGY INSTITUTE

Alexander Marion
DIRECTOR, ENGINEERING
NUCLEAR GENERATION DIVISION

April 22, 2002

Mr. Gary M. Holahan
Director, Division of Systems, Safety and Analysis
Office of Nuclear Reactor Regulation
Mail Stop O10-A1
U. S. Nuclear Regulatory Commission
Washington, DC 20555-0001

SUBJECT: EPRI Report TR-1002865, *Topical Report on Reactivity Initiated Accidents: Bases for RIA Fuel Rod Failures and Core Coolability Criteria*

PROJECT NUMBER: 689

Dear Mr. Holahan:

The NRC has emphasized the importance of developing a risk-informed analysis approach for extended burn up submittals and has looked to the industry to take the lead in developing the criteria and supporting bases that would be applied to new fuel designs proposed for extended burn up application. In response, the EPRI Robust Fuel Program has developed and is implementing a process for determining licensing criteria for extended burn up application. This process, titled "Licensing Criteria for Fuel Burn up Extensions Beyond 62 GWd/tU-Industry Guide, Revision 5," was discussed with NRC staff at a December 6, 2000, meeting on high burn up fuel issues. The initial application of this process has focused on criteria that would be applicable to reactivity initiated accidents (RIA).

The enclosed topical report, EPRI TR-1002865, *Topical Report on Reactivity Initiated Accidents: Bases for RIA Fuel Rod Failures and Core Coolability Criteria*, describes the technical bases supporting a set of revised acceptance criteria for use in the safety analysis of the hot-zero power and hot-full power RIA in both pressurized and boiling water reactors. This document is submitted for NRC review and endorsement for application to advanced fuel designs intended for extended burn up use.

The enclosed report, while final, is marked as draft pending completion of the EPRI publication process. Copies of the publication version of the report will be provided to you when they become available.

D046

1776 I STREET, NW SUITE 400 WASHINGTON, DC 20006-3708 PHONE 202.739.8080 FAX 202.533.0164 am@nei.org

Public
per NRC

Tie to NRC Performance Goals

This topical report is of importance to over 75 domestic operating reactors. The NRC staff review is considered to be relevant to the NRC performance goals as identified below.

(1) Maintain Safety

Safety is maintained through the establishment of a clear, technically based tie between licensing criteria and the applicable regulatory requirements to be met by fuel licensed for operation beyond 62 GWd/tU.

(2) Maintain Public Confidence

Public confidence will be maintained through the development, review and subsequent use of a more scrutable process that clearly identifies the manner and basis for demonstrating that reactor fuel can be operated at higher fuel burn up levels.

(3) Improve Efficiency and Effectiveness of Regulation

Efficiency and effectiveness of regulation will be improved. The establishment of a single comprehensive set of licensing criteria that can be used by licensees; fuel vendors and NRC will serve to promote increased review efficiency and will enable a reduction in overall costs to industry.

(4) Reduce Unnecessary Burden

The development and approval of the licensing criteria to be applied to high burn up fuel will reduce unnecessary regulatory burden in two ways. First, the upfront identification of the criteria against which new fuel applications will be reviewed enables licensees and fuel vendors to more easily plan licensing and regulatory interactions we anticipate that the use of technically based licensing criteria will help to streamline the review and approval process.

Basis for Request for Waiver of Part 170 Fees

We believe any NRC staff review of the topical report should be exempt from the fee recovery provision contained in 10 CFR Part 170. This submittal provides information that might be helpful to NRC staff when evaluating licensee and fuel vendor submittals intended to achieve approval of extended fuel burn up limits. Consequently, such reviews are exempt under §170.21, Schedule of Facility Fees. Footnote 4 to the Special Projects provision of §170.21 states, "Fees will not be

assessed for requests/reports submitted to the NRC...[a] s means of exchanging information between industry organizations and the NRC for the purpose of supporting generic regulatory improvements or efforts."

We are prepared to meet with you and your staff to discuss further details for the review and approval of the topical report. Please contact John Butler 202-739-8108, jcb@nei.org or me, 202-739-8080, am@nei.org, to discuss how best to proceed forward with the review.

Sincerely,

Alex Marion

Alexander Marion

JCB/maa
Enclosure

c: Mr. Peter Wen, U. S. Nuclear Regulatory Commission
Mr. Jared Wermiel, U. S. Nuclear Regulatory Commission
Mr. Ralph Caruso, U. S. Nuclear Regulatory Commission
Dr. Rosa Yang, EPRI

EPRI

Topical Report on Reactivity Initiated Accident: Bases for RIA Fuel Rod Failure and Core Coolability Criteria

Topical Report on Reactivity Initiated Accident: Bases for RIA Fuel Rod Failure and Core Coolability Criteria

1002865

Draft Report Rev. 2, April 2002

EPRI Project Manager
R. Yang

EPRI • 3412 Hillview Avenue, Palo Alto, California 94304 • PO Box 10412, Palo Alto, California 94303 • USA
800.313.3774 • 650.855.2121 • askepri@epri.com • www.epri.com

DISCLAIMER OF WARRANTIES AND LIMITATION OF LIABILITIES

ORGANIZATION(S) THAT PREPARED THIS DOCUMENT

ANATECH Corp.

ORDERING INFORMATION

Requests for copies of this report should be directed to the EPRI Distribution Center, 207 Coggins Drive, P.O. Box 23205, Pleasant Hill, CA 94523, (800) 313-3774.

CITATIONS

This report was prepared by

ANATECH Corp.
5435 Oberlin Drive
San Diego, CA 92121

Principal Investigator
R. O. Montgomery

EPRI
3412 Hillview Avenue
Palo Alto, CA 94304

Principal Investigator
Nicolas Waeckel
Rosa Yang

This report describes research sponsored by EPRI.

The report is a corporate document that should be cited in the literature in the following manner:

Topical Report on Reactivity Initiated Accident: Bases for RIA Fuel Rod Failure and Core Coolability Criteria, EPRI, Palo Alto, CA: 2002. 1002865.

SUMMARY

S.1 Scope of Report

The purpose of this topical report is to describe the technical bases supporting a set of revised acceptance criteria for use in the safety analysis of the hot-zero power (HZP) and hot-full power (HFP) Reactivity Initiated Accidents (RIA) in Pressurized Water Reactors (PWRs) and Boiling Water Reactors (BWRs). The primary RIA events considered in this topical report are the postulated control rod ejection accident (REA) for PWRs and the postulated control rod drop accident (RDA) for BWRs. The revised RIA acceptance criteria have been developed as part of the on-going industry effort to extend fuel rod average burnup levels beyond the current limit of 62 GWd/MTU.

The revised acceptance criteria are shown in Figure S-1 and are defined in terms of the radial average peak fuel enthalpy and as a function of rod average burnup. Two separate criteria have been developed to 1) ensure long-term cooling of the reactor core after the accident and 2) account for radiological release to the environment following cladding failure. The strategy to develop two separate criteria is consistent with the approach in Regulatory Guide 1.77 which contains a limit on the maximum radial average fuel enthalpy to satisfy the requirements of 10 CFR 50 Appendix A – General Design Criterion 28 and a threshold to estimate the number of fuel rod failures.

The curves shown in Figure S-1 are applicable to:

- PWR: HZP and HFP REA
- BWR: HZP RDA
- Cladding materials: Zircaloy-4, Zircaloy-2, ZIRLO and M5
- UO_2 or UO_2-Gd_2O_3 fuel rods operated up to a target lead rod average burnup of 75 GWd/MTU
- PWR fuel rod designs: 17x17, 15x15, and 14x14
- BWR fuel rod designs: 8x8, 9x9, and 10x10
- Maximum cladding outer surface oxide thickness layers less than 100 microns
- No fuel rods with cladding outer surface oxide spallation sufficient to have a significant affect on the cladding mechanical properties

The revised RIA fuel rod failure threshold is applicable to advanced cladding designs provided the cladding material exhibits superior or equivalent ductility as Zircaloy cladding with the same outer surface oxide layer thickness. Since the development approach used material properties and corrosion rates based on low-Sn Zircaloy-4, the fuel rod failure threshold shown in Figure S-1 represents a lower bound for advanced fuel rod designs using low corrosion alloys. Application of the revised acceptance criteria to cladding material not addressed in the topical report will require the development of mechanical property data to demonstrate that the ductility relations used to derive the criteria represent a lower bound for the new cladding material.

As part of the limited scope LTA program to collect data at extended burnup (WCAP-15604-NP), industry surveillance programs will be used to demonstrate that the maximum oxide thickness data is bounded by the 100 micron oxide thickness value limit used to develop the fuel rod failure threshold.

The revised acceptance criteria shown in Figure S-1 are for use in the design basis analysis of the PWR REA and the BWR RDA to account for the number of estimated fuel rod failures and to demonstrate that the reactor core geometry remains amenable to cooling following the hypothetical accident. The method to utilize these criteria in the design basis methodology is as follows:

a) An accepted neutron kinetics analysis method is used to calculate the maximum deposited energy as a function of rod average burnup.

b) The radial average peak fuel enthalpy is calculated using an accepted fuel rod thermal analysis methodology

c) The radial average peak fuel enthalpy as a function of rod average burnup is compared to the fuel failure threshold shown in Figure S-1. All rods exceeding the fuel rod failure threshold should be considered failed.

d) The calculated radial average peak fuel enthalpy as a function of rod average burnup should be compared to the core coolability limit shown in Figure S-1. No fuel rods will have a maximum radial average peak fuel enthalpy that exceeds the limit shown in Figure S-1.

It is envisioned that the NRC will review the technical bases for the revised acceptance criteria and adopt them as generic criteria applicable to the design basis analysis of RIA events. One method to achieve generic usage of these criteria will be to use the technical bases described in this topical report to modify the appropriate sections in Regulatory Guide 1.77 and the Standard Review Plan Section 4.2.

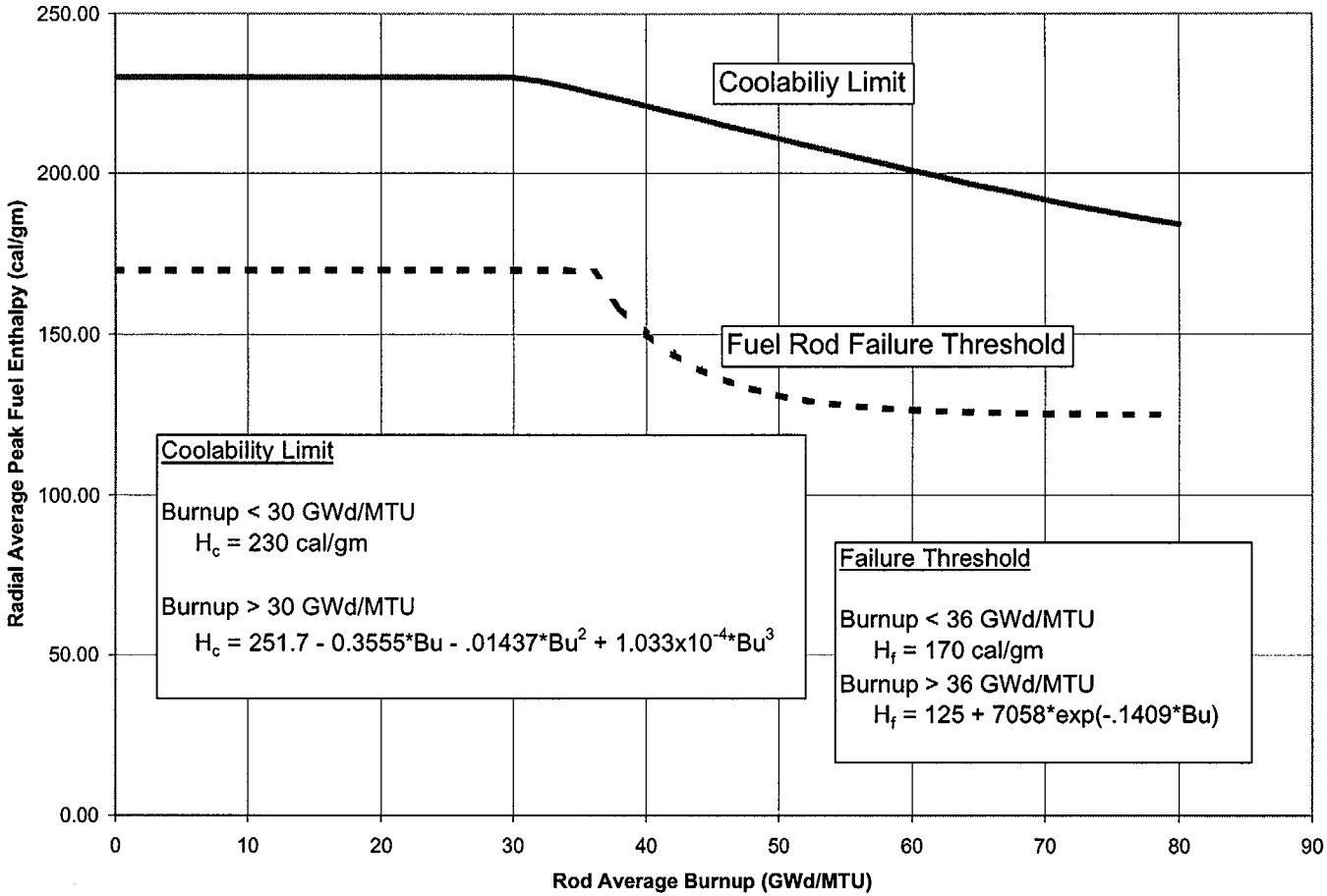

Figure S-1
Revised Acceptance Criteria for the PWR REA and BWR RD events. The criteria are defined in terms of the radial average peak fuel enthalpy as a function of rod average burnup.

S.2 Approach to Develop Revised Acceptance Criteria

The approach to develop the revised criteria used an evaluation methodology that combined both experimental data and analytical calculations to establish the influence of burnup on transient fuel rod behavior during reactivity initiated accidents. Used in the evaluation were experimental data from RIA-simulation tests on fuel segments extracted from commercial UO_2-Zircaloy cladding fuel rods irradiated to 64 GWd/MTU. These technical bases were then translated to the PWR REA application using the state-of-the-art fuel rod behavior analysis code FALCON as a means to establish the fuel rod failure threshold and core coolability limit as a function radial average fuel enthalpy and rod average burnup. The advantage of using a combined approach of analytical evaluations and experimental data to derive the revised acceptance criteria is that the methodology can be applied to other fuel rod designs and cladding materials to determine application specific criteria, if relaxation of the criteria is required.

To assure core coolability and to preclude damage to the reactor pressure vessel, a core coolability limit is established based on the maximum radial average peak fuel enthalpy that precludes incipient UO_2 pellet melting during power deposition. The fuel enthalpy required to produce incipient pellet melting was determined using a FALCON analysis to calculate the peak fuel pellet temperature as a function of both radial average peak fuel enthalpy and rod average burnup. The analytical approach considered the following effects:

- The influence of burnup on the UO_2 melting temperature
- Local power, burnup and temperature peaking
- Heat conduction from the pellet to the cladding
- Burnup-induced fuel-cladding gap closure
- The influence of burnup on the UO_2 thermal conductivity

The results of spatial kinetics analyses for both PWR and BWR RIA events show that the power pulse width will be greater than 10 milliseconds for typical power pulses. Experimental data demonstrate that the dispersal of finely fragmented solid pellet material occurs at pulse widths less than 10 milliseconds. However, limiting the peak fuel temperature in the rim to the melting temperature insures that most of the pellet material is well below the melting temperature in high burnup fuel. Such a restriction on the maximum radial average peak fuel enthalpy mitigates any significant consequences in the unlikely event that finely fragment solid pellet material is dispersed into the coolant.

Second, a threshold on the radial average peak fuel enthalpy is defined that represents the occurrence of fuel rod failure for use in off-site dose calculations. The fuel rod failure threshold below a rod average burnup of 36 GWd/MTU is established to preclude cladding failure by high temperature processes such as oxidation-induced embrittlement or clad ballooning and rupture. Experimental data from both RIA-simulation tests and power-coolant mismatch tests that operated in post-DNB heat transfer were used to justify a radial average peak fuel enthalpy below which peak cladding temperatures remained below the time-at-temperature threshold for oxidation-induced cladding embrittlement failure. Furthermore, experimental data from NSRR and IGR/BIGR were used to demonstrate that a positive pressure differential in excess of 1 MPa

at the start of the RIA event is required to cause ballooning and rupture in both Zircaloy and Zr-niobium alloys. At HZP conditions, it can be shown that the fuel rod internal pressure is less than the coolant pressure for low and intermediate burnup fuel rods, thus eliminating any potential for fuel rod failure by ballooning and rupture.

Beyond a rod average burnup of 36 GWd/MTU, the fuel rod failure threshold is based on cladding failure by pellet-cladding mechanical interaction (PCMI). The approach used a realistic evaluation of the fuel rod response during a RIA power pulse combined with a conservative estimation of the cladding ductility decrease with burnup to establish the fuel rod failure threshold. The FALCON PCMI analysis included the following effects:

- Pellet-cladding gap closure as a function of burnup
- Pellet to cladding heat conduction
- Cladding to coolant heat transfer
- Local power, burnup and temperature peaking
- Influence of burnup on the UO_2 thermal conductivity
- Pellet thermal expansion, cracking and plastic deformation
- Cladding elastic and plastic deformation

Cladding failure was established using the Critical Strain Energy Density (CSED) approach to describe the effects of irradiation and cladding outer surface oxidation on the cladding ductility. An upper bound cladding outer surface oxidation rate for low-Sn Zircaloy-4 was used in the evaluation to ensure conservatism in the failure threshold. The result is a lower bound fuel rod failure threshold as a function of rod average burnup.

ACRONYMS

BWR	Boiling Water Reactor
CABRI	French Test Reactor
CDC	Capsule Driver Core (at SPERT)
CEA	Commissariat a l' Energie Atomique (France)
CSED	Critical Strain Energy Density
CZP	Cold-Zero Power
DNB	Departure from Nucleate Boiling
DNBR	Departure from Nucleate Boiling Ratio
EdF	Elecricité de France
EOL	End of Life
EPRI	Electric Power Research Institute
ESCORE	EPRI Steady State Core Reload Evaluation Code
FALCON	Fuel Analysis & Licensing Code
FCI	Fuel-Coolant Interaction
FRAPTRAN	Fuel Rod Analysis Program, Transient
FREY	Fuel Rod Evaluation System
FSAR	Final Safety Analysis Report
FWHM	Full Width Half Maximum
HFP	Hot-Full Power
HZP	Hot-Zero Power
IFBA	Integral Fuel Burnuable Absorbers

IPSN	Institute for Protection and Nuclear Safety (France)
JAERI	Japan Atomic Energy Research Institute (Japan)
LOCA	Loss-of-Coolant Accidents
LWR	Light Water Reactor
MOX	Mixed Oxide Fuel
NB	Nuclear Boiling
NRC	Nuclear Regulatory Commission
NSRR	Nuclear Safety Research Reactor
PBF	Power Burst Facility (U. S.)
PCMI	Pellet-Cladding Mechanical Interaction
PIRT	Phenomena Identification & Ranking Table
PROMETRA	Program for Measuring the Mechanical Properties of the Cladding
PWR	Pressurized Water Reactor
RDA	Rod Drop Accident
REA	Rod Ejection Accident
REP	Pressurized Water Reactor (rectur a eau pressurisie)
RIA	Reactivity Initiated Accidents
SED	Strain Energy Density
SCANAIR	Code for describing the fuel behavior under an RIA Transient
SPERT	Special Power Excursion Reactor Test (U. S.)
TRANSURANUS	European Institute for Transuranium Element Fuel Rod Performance Code
TUBRNP	TRANSURANUS Burnup Model
UE	Uniform Elongation

CONTENTS

LIST OF FIGURES

LIST OF TABLES

1
INTRODUCTION

1.1 Background

The goal to achieve higher fuel rod burnup levels has produced considerable interest in the transient response of high burnup fuel. The database on transient fuel behavior is limited at burnup levels beyond 40 GWd/tU and is based on older fuel rod designs. Several experimental programs are currently underway to generate data on the behavior of high burnup fuel under transient conditions representative of Loss-of-Coolant Accidents (LOCA's) and Reactivity Initiated Accidents (RIA's) [Chung et al. 1996; Papin et al.1996; Fuketa et al.1996][1]. Such programs include the RIA simulation experiments performed at the CABRI facility in France and the Nuclear Safety Research Reactor (NSRR) in Japan. The purpose of these programs is to provide data that can be used to develop safety criteria for extended burnup levels applications and to validate analytical codes for high burnup fuel behavior.

The initial results from RIA-simulation tests on fuel rod segments with burnup levels above 50 GWd/tU, namely CABRI REP Na-1 (1993) and NSRR HBO-1 (1994), raised concerns that the existing licensing criteria defined in NUREG-0800 may be inappropriate beyond a certain level of burnup. As a consequence, EPRI and the nuclear industry conducted an extensive review and assessment of the observed behavior of high burnup fuel under RIA conditions which was summarized in EPRI TR-106387 [Montgomery and Rashid 1996; Ozer et al. 1996; Montgomery et al. 1997a] The objective of this program was to conduct a detailed analysis of the data obtained from RIA-simulation experiments and to evaluate the applicability of the data to commercial LWR fuel behavior during a REA or CRDA. The industry assessment included a review of the fuel segments used in the tests, the test procedures, in-pile instrumentation measurements, post-test examination results, and a detailed analytical evaluation of several key RIA-simulation tests using the EPRI-sponsored transient fuel behavior code FREY, which was an earlier version of the FALCON transient code used in this evaluation. Major conclusions from that industry assessment are:

- The RIA-simulation test conditions are not representative of those expected during a postulated in-reactor REA or CRDA. The experiments were conducted either in room-temperature, atmospheric-pressure water or in hot sodium coolant. The pulses were considerably more rapid (sharper and narrower) than anticipated LWR power pulses calculated using 3-D spatial kinetics methods.
- In many cases, the conditions under which the test rods were base-irradiated produced cladding corrosion and hydriding features that were not representative of commercial LWR

[1] References provided in brackets [ ] are listed in alphabetical order in Section 6.

fuel. This was most evident in early tests performed in SPERT-CDC and the JM Test Series in the NSRR facility

- Analytical evaluations and separate effects data are required to understand the key mechanisms operative in RIA-simulation tests and to translate the experimental results to LWR conditions and different cladding materials.
- Loss of cladding ductility due to localized hydrides was the major cause of failure for high burnup test rods during the RIA-simulation tests. Although, loss of cladding ductility may be a result of higher burnup, the causes are more related to adverse hydride content and distributions resulting from outer surface cladding oxidation anomalies such as spallation. The primary effect of burnup is to increase PCMI by gap closure effects such as solid fission product swelling.

Since the publication of EPRI TR-106387, the industry has continued the assessment and evaluation of the burnup impact on the behavior of high burnup fuel during a RIA. More recent RIA-simulation experiments have been conducted on high burnup PWR and BWR test rods and the analytical evaluations and post-test examinations have provided further insights into the behavior of high burnup fuel under transient conditions. The newer data continue to confirm the major conclusions summarized above. It is becoming apparent that our understanding of high burnup fuel behavior during a RIA event is sufficient and that most post-test observations can be explained.

As a logical next step in the process, Working Group 2 of the EPRI Robust Fuel Program, representing the nuclear industry, has developed a strategy to resolve the RIA licensing issues raised by the RIA-simulation experiments. The Industry strategy consists of: 1) development of revised RIA licensing criteria using experimental data and analysis methods, and 2) development of improved neutron kinetics methods to demonstrate compliance to the revised licensing criteria.

The approach employed to develop the revised licensing criteria by the Industry combines elements of experimental results and analytical evaluations to establish a fundamental understanding of fuel behavior during RIA events. The approach includes three major components:

1. Establish the transient behavior of intermediate and high burnup fuel rods using well-characterized RIA simulation tests. The RIA-simulation experiments in the previous evaluation, and the more recent tests on rods with burnup levels ranging from 45-65 GWd/MTU in the CABRI, NSRR and IGR/BIGR reactors, provide a database of in-pile observations and post-test examinations that can be used to evaluate the phenomena and mechanisms that influence the transient performance of the fuel and cladding. A summary of the RIA-simulation database is provided in Section 2.2

2. Define the cladding mechanical properties using data from separate effects tests. The database of Zircaloy cladding mechanical properties furnishes insights into the influence of irradiation damage, hydrogen content and distribution, and temperature on the capability of the cladding to accommodate the pellet loading during an RIA event. The database of

separate effects tests on Zircaloy cladding mechanical properties is described in Section 2.3, as well as the methods used to develop a cladding integrity model.

3. Benchmark the RIA analysis capabilities in the transient fuel behavior code FALCON using experimental data from the database of RIA-simulation tests. FALCON, which is the most recent version of the FREY transient fuel behavior code, calculates the thermal and mechanical performance of a single fuel rod during transient power conditions. Performing fuel rod analyses of the RIA experiments provides a means to validate the predictive capabilities of the program and also provides insights into the mechanisms that influence the pellet and cladding transient performance. A description of FALCON and the fuel rod analyses performed using the code is included in Section 2.4.

This comprehensive approach has provided some key results: 1) a mechanistic basis for understanding the key phenomena that are operative in RIA-simulation tests and 2) qualified the use of FALCON for the translation of non-prototypical RIA-experimental results to both LWR conditions and different cladding materials. The industry has used the technical insights gained from this deterministic evaluation as the basis for developing the proposed revisions to the regulatory criteria used in the licensing analysis of RIA events. As will be discussed in this report, the proposed regulatory criteria are a combination of the best-estimate technical understandings of transient fuel behavior coupled with conservative assumptions to account for the uncertainties associated with high burnup fuel.

In addition to proposing revised RIA licensing criteria, Working Group 2 has also developed a new methodology for analyzing the PWR rod ejection accident based on a three-dimensional neutron kinetics approach. This methodology is intended to serve as a template, which the industry can follow in upgrading their analytical methods. Improvements in the compliance methodology are expected to be necessary to meet the revised regulatory criteria which unlike the existing criteria will decrease as a function of rod average burnup. A separate EPRI report will be submitted to the NRC to obtain generic review and approval of the methodology.

Combined with the NRC Phenomena Identification and Ranking (PIRT) review conducted on the PWR REA event, the technical assessment performed by the industry establishes a strong technical basis to develop revised licensing criteria for reactivity initiated accidents. The development of additional RIA test data will slow for the next several years as the CABRI facility is modified and upgraded to include a Water Loop [Papin et al. 2000]. Given that our current understanding of the important mechanisms is sufficient, it is appropriate at this time to propose revised licensing criteria for RIA events. The additional RIA-simulation tests on high burnup fuel rods with advanced cladding alloys planned as part of the International CABRI Water-Loop project and the NSRR test program will provide data at extended burnup and with advanced cladding materials that can be used to confirm the proposed regulatory criteria.

1.2 Scope of Topical Report

The focus of this report is to summarize the technical bases for the revised core coolability criteria and fuel rod failure threshold used in the licensing analysis of a PWR or BWR HZP and HFP RIA events. Section 2 summarizes the regulatory bases associated with reactivity initiated

accidents, provides a review of the experiments performed to evaluate the behavior of irradiated fuel to RIA conditions, reviews the mechanical property tests used to describe the performance of irradiated cladding, and finally, summarizes the validation of the fuel rod analysis methodology used to analyze and interpret the RIA experiments. Section 3 summarizes the current technical understanding of the fuel rod failure mechanisms during RIA transient conditions and describes the methodology used to develop the proposed fuel rod failure threshold. Section 4 summarizes the issues associated with maintaining core coolability and describes the approach used to develop the proposed core coolability limit.

2
DATABASE REVIEW

Section 2 summarizes the current licensing and technical bases related to RIA events. Included is a review of the regulatory background for the current licensing criteria, a review of the RIA-simulation test database, a review of the separate effects tests used to establish the mechanical behavior of high burnup cladding material, and a review of the RIA test analysis performed using FALCON.

2.1 Regulatory Basis

Section 4.2 of NUREG-0800 - Standard Review Plan for the Review of Safety Analysis Reports for Nuclear Power Plants (SRP) specifies two licensing criteria applicable to RIA events: a fuel coolability limit and a fuel rod failure threshold [U. S. Nuclear Regulatory Commission, 1981]. The fuel coolability limit was established to restrict the amount of energy deposition into the fuel rod during an RIA event as a means to preclude fuel melting, fragmentation and dispersal. Under certain conditions, the mechanical energy release resulting from dispersal of molten fuel material may be sufficiently large to destroy the cladding and the fuel assembly geometry and produce significant pressure pulses in the primary system. The fuel rod failure threshold was established to meet the requirements of fission product release during postulated accidents. The regulatory and technical bases for these criteria are outlined below.

2.1.1 Fuel Coolability Limit (Violent Expulsion of Fuel)

The fuel coolability limit was developed to satisfy regulatory requirements contained in General Design Criteria 28 (10 CFR Part 50 Appendix A). GDC 28 defined in 10 CFR Part 50 Appendix A specifies that reactivity control systems shall be designed to assure that the effects of a postulated reactivity accident neither (1) result in damage to the reactor coolant pressure boundary greater than limited local yielding, nor (2) sufficiently disturb the core, its support structures, or other reactor pressure vessel internals to cause serious impairment of core cooling capability. GDC 28 further specifies that reactivity initiated accidents shall include consideration of rod ejection (unless prevented by positive means), rod drop, steam line rupture, changes in coolant temperature and pressure, and cold water addition.

Regulatory Guide 1.77, "Assumptions Used for Evaluating a Control Rod Ejection Accident for Pressurized Water Reactors," outlines the acceptable assumptions and analytical methods that may be used in evaluating REAs for PWRs. Furthermore, Regulatory Guide 1.77 states that by using these assumptions and methods it should be shown that:

1. Reactivity excursions will not result in a radial average fuel enthalpy greater than 280 cal/g at any axial location in any fuel rod.

2. Maximum reactor pressure during any portion of the assumed transient will be less than the value that will cause stresses to exceed the Emergency Condition stress limits as defined in Section III of the ASME Boiler and Pressure Vessel Code.

Standard Review Plan Section 4.2 paragraph II.A.3.b also states that the PWR and BWR fuel coolability limit for violent expulsion of fuel should be a limit of 280 cal/gmUO_2 on the radial average peak fuel enthalpy.

The radial average peak fuel enthalpy limit of 280 cal/gUO_2 is based on a Regulatory staff review of the available data (prior to 1974) from the SPERT and TREAT experimental programs describing the fuel failure consequences following a high rate of reactivity insertion [Martinson and Johnson 1968; Miller and Lussie 1969; USAEC 1974]. The review found that there exists a potential at high fuel energy depositions for prompt rupture of a fuel rod and the rapid heat transfer from finely dispersed molten fuel material. Prompt fuel element rupture is defined in Regulatory Guide 1.77 as a rapid increase in internal fuel rod pressure due to extensive fuel melting, followed by rapid fragmentation and dispersal of molten fuel and cladding material into the coolant. The review concluded that the failure consequences of UO_2 fuel rods were insignificant for total energy depositions below 300 cal/g for both unirradiated and irradiated fuel rods. As a result, a peak radially averaged fuel enthalpy of 280 cal/g was considered to be a conservative maximum limit to ensure that core damage will be minimal and that both short-term and long-term core cooling capability will not be impaired.

The fuel coolability limit of 280 cal/gm for the maximum radial averaged peak fuel enthalpy, defined in Reg. Guide 1.77, was defined based on experiments performed on unirradiated test rods that experienced severe fuel and clad melting during the energy deposition. MacDonald, et. al. performed a review and re-assessment of the supporting data and found that although, the limit for violent expulsion of fuel is stated in terms of radial average peak fuel enthalpy, the data used to establish the limit was actually based on the total energy deposition for the tests [MacDonald et al. 1980]. The maximum radially averaged fuel enthalpy is less than the associated total energy deposition due to heat conduction from the fuel and energy deposition from delayed neutrons. Re-evaluation by MacDonald, et. al. of the tests performed in the SPERT and TREAT facilities using the maximum radially averaged fuel enthalpy shows that the consequences for enthalpies greater than 250 cal/gm were fragmentation and loss of rod geometry. These observations indicate that the 280 cal/gm may not be conservative with respect to maintaining fuel coolability. Based on the earlier re-evaluation, a revision of the fuel coolability limit to 230 cal/gm for the maximum radial average peak fuel enthalpy would provide margin to loss of rod geometry and would be a more limit appropriate at zero and low burnup (< 10 GWd/MTU).

2.1.2 Fuel Rod Failure Threshold (Excessive Fuel Enthalpy)

The fuel rod failure threshold for RIA events is specified in SRP Section 4.2 (II.A.2.f) and was established to meet the requirements of 10 CFR Part 100.11 and 10CFR50 Appendix A, GDC-19

as these relate to both on-site and off-site dose consequences. The fission product release resulting from fuel rod failure during a postulated accident is required by 10 CFR Part 100.11 to calculate the radiation dose for the exclusion area boundary (EAB) and low population zone (LPZ) boundary. Regulatory Guide 1.77 specifies that the offsite dose levels at the EAB and LPZ for an RIA event must be well within the exposure guideline values in 10 CFR Part 100.11. Appendix A of Standard Review Plan section 15.4.8 and 15.4.9 defines "well within" as 25% of the 10 CFR 100.11 exposure guidelines. The assumptions used in calculating the source term activity for fuel rod failure are defined in Reg. Guide 1.77 Appendix B. For fuel rod failure, the accumulated fuel-cladding gap activity should be assumed to be 10% of the iodines and 10% of the noble gases accumulated at the end of core life, assuming continuous maximum full power operation. The activity inventory should take no allowance for radioactive decay prior to the accident.

The fuel rod failure threshold for PWR and BWR applications is as follows:

PWR

> Regulatory Guide 1.77 states "The number of fuel rods experiencing clad failure should be calculated and used to obtain the amount of contained fission product inventory released to the reactor coolant system." Clad failure should be assumed to occur when the calculated heat flux equals or exceeds the departure from nucleate boiling ratio (DNBR) for zero power, low power and full power RIA events in PWRs.

BWR

> The fuel rod failure threshold used in BWR's is defined in Standard Review Plan Sections 4.2 II.A.2.f) and 15.4.9. Cladding failure should be assumed for rods that experience a maximum radially averaged fuel enthalpy greater than 170 cal/g for RDA events initiated from zero or low power. The fuel enthalpy threshold for cladding failure established for zero or lower power RDAs was defined to be a surrogate for the Critical Power Ratio threshold traditionally used for BWR clad overheating. As will be seen in Section 2.2, zero or lower burnup fuel rods tested above 170 cal/g experienced clad overheating and subsequent cladding fracture following quenching. For rated power conditions, fuel rods that experience cladding dryout should be assumed to fail.

2.2 RIA Simulation Test Database

Experimental programs have been conducted worldwide since the early 1960's to evaluate fuel behavior during rapid energy deposition simulating a reactivity accident. Prior to the late 1980's. all of the relevant RIA simulation experiments were conducted in the US or Japan. In the US, the two main programs were the SPERT-CDC and the PBF RIA tests [Martinson and Johnson 1968; Miller 1970; MacDonald 1980]. The experiments in Japan were conducted by JAERI in the NSRR facility. The early RIA simulation tests in the US and Japan consisted of experimental programs on unirradiated tests rods or low burnup (< 30 GWd/MTU) test rods specially fabricated for testing and were pre-irradiated in material test reactors such as the Engineering Test Reactor [Miller 1970; Miller 1971] or the Japanese Materials Test Reactor [Ishikawa 1980; Fuketa 1997]. A primary goal of a majority of these tests was to investigate the post-failure

consequences leading to coolant pressure pulse generation. As a consequence, these test rods were fabricated with reduced rod diameters and high ^{235}U enrichments to achieve high levels of energy deposition. Also, the pre-irradiation was accelerated to obtain the desired burnup in the shortest time possible. These conditions introduced complexities that make application of the data to modern LWR fuel rod conditions difficult. As a result, most of these data are only applicable to zero burnup.

More recently, three experimental programs have been conducted to evaluate the behavior during RIA conditions of irradiated fuel rods from commercial reactors. These programs include the CABRI REP Na tests in France [Schmitz and Papin 1998; MacLachlan 2000a; MacLachlan 2000b], the NSRR tests in Japan [Fujishiro 1992; Fuketa 1996; Fuketa 1998; Fuketa 1999; Fuketa 2000], and the IGR/BIGR tests in Russia [Yegorova 1999; Bibilashvili et al. 2000]. A total of sixty-one (61) RIA simulation tests have been conducted on LWR-type test rods in the burnup range between 26-65 GWd/tU, including twenty-nine tests on PWR-type fuel rods, fourteen tests on BWR-type fuel rods, four tests on PWR MOX-type fuel rods, and fourteen tests on VVER-type fuel rods. These tests were performed in sodium coolant (280°C and 0.5 MPa) in the CABRI program or in stagnant water (25°C and 0.1 MPa) conditions in the NSRR and IGR/BIGR programs. All of the test rods were refabricated into short segments from full-length fuel rods extracted from fuel assemblies that had been irradiated in commercial PWR, BWR, or VVER power plants.

A summary of the most recent RIA simulation tests conducted using test rods from commercial fuel rods is shown in Table 2-1 through 2-4 for the CABRI, NSRR, and IGR/BIGR programs. A more detailed database of RIA experiments, including zero burnup tests in the US and Japan is contained in Appendix A.

Tables 2-1 through 2-4 highlight most of the key features of each experiment. The test segment burnup and oxide thickness are provided to describe the condition of the test rods. The fuel rod design and the pellet type (UO_2 vs. MOX) are also indicated in each table to show the wide variety of fuel designs tested. The two key parameters that define the power pulse characteristics namely, pulse width and maximum radial average fuel enthalpy (H_{max}), are also provided for each test. Finally, test results described by the fuel enthalpy at cladding failure (H_f) and the occurrence of fuel dispersal are provided for those tests that failed. In most cases, the fuel enthalpy at failure was obtained from in-pile instrumentation and the presence of fuel dispersal was determined by post-test examination techniques.

The attributes used to define an RIA experiment include the total energy deposition (E_p) and the maximum radial average fuel enthalpy (H_{max}). Normally, the result of RIA simulation experiments are reported in terms of E_p, which is obtained from the neutron physics analysis of post-test destructive examinations. The total energy deposition includes three components: the energy produced by prompt fissions during the power pulse, the energy from delayed neutron fissions, and the γ- and β-decay from fission products. The last two sources are the delayed energy components that occur during the power runout before reactor scram and therefore are not important contributors to the prompt fuel rod response. Unfortunately, the reporting of total deposited energy has not been consistent between the different test programs. Some organization report the prompt energy deposition, others have reported the total deposited energy, including

the delayed energy deposition. This makes it difficult to compare the results reported from the different programs.

The maximum radial average fuel enthalpy is also determined by three components: the initial (or baseline) fuel enthalpy, the prompt energy deposition, and the amount of heat conduction that occurs during the power pulse. The maximum radial average fuel enthalpy is obtained through a fuel rod analysis that accounts for the heat condition characteristics of the test rod and the rate of energy deposition. For power pulses with pulse widths of 10 milliseconds or less, the effect of heat conduction is minor and the maximum radial average fuel enthalpy is near the sum of the initial enthalpy (H_i) and the prompt energy deposition. Heat conduction effects become more prevalent for pulse widths greater than 20 milliseconds.

It should be noted that for tests at 280°C (CABRI), the initial fuel enthalpy is 16-17 cal/gm. For tests performed at atmospheric conditions (SPERT-CDC, NSRR). The initial fuel enthalpy is approximately zero.

The schematic in Figure 2-1 highlights the relationships between the power pulse, the energy deposition and the radial average fuel enthalpy. The energy deposition represents the integration of the power-time curve and reaches the total energy deposited once the power returns to zero. The radial average fuel enthalpy is calculated based on the UO_2 specific heat and the radial temperature profile. A maximum is reached near the late part of the power pulse as heat conduction effects begin to dominate. The relative response of these different parameters depends on the pulse width defined by the full-width half maximum (FWHM) of the power pulse.

Figure 2-2 contains a plot of the RIA-simulation tests from the US (CDC-SPERT/PBF), France (CABRI), and Japan (NSRR). Included in Figure 2-2 are several experiments from the database shown in Appendix A conducted on non-commercial test rods as well as test rods from commercial LWR fuel rods listed in Table 2-1 through 2-4. The maximum radial average peak fuel enthalpy is plotted as a function of the test rod burnup for more than 80 tests. Those tests that experienced cladding failure are indicated by a solid symbol and are plotted at the radial average fuel enthalpy at failure. The data show a general downward trend that is caused by a decrease in test segment reactivity with burnup. As shown in Figure 2-2, the rods that experienced cladding failure are interspersed amongst the rods where the cladding remained intact following the power pulse. Because of the fact that the failed and non-failed rods are interspersed when plotted as a function of burnup indicates that burnup is not the sole parameter that influences the cladding integrity, other parameters such as cladding temperature, the level of zirconium oxidation, and the cladding zirconium hydride content and distribution may also have an impact.

An extensive review and assessment of the test results developed in these experimental programs up to 1996 has been performed by the nuclear industry and reported in EPRI TR-106387. Since that review, additional tests have been conducted in these programs and the summary discussions below will highlight the results of these additional tests [Schmitz and Papin 1998; Fuketa 1998; Fuketa, 2000].

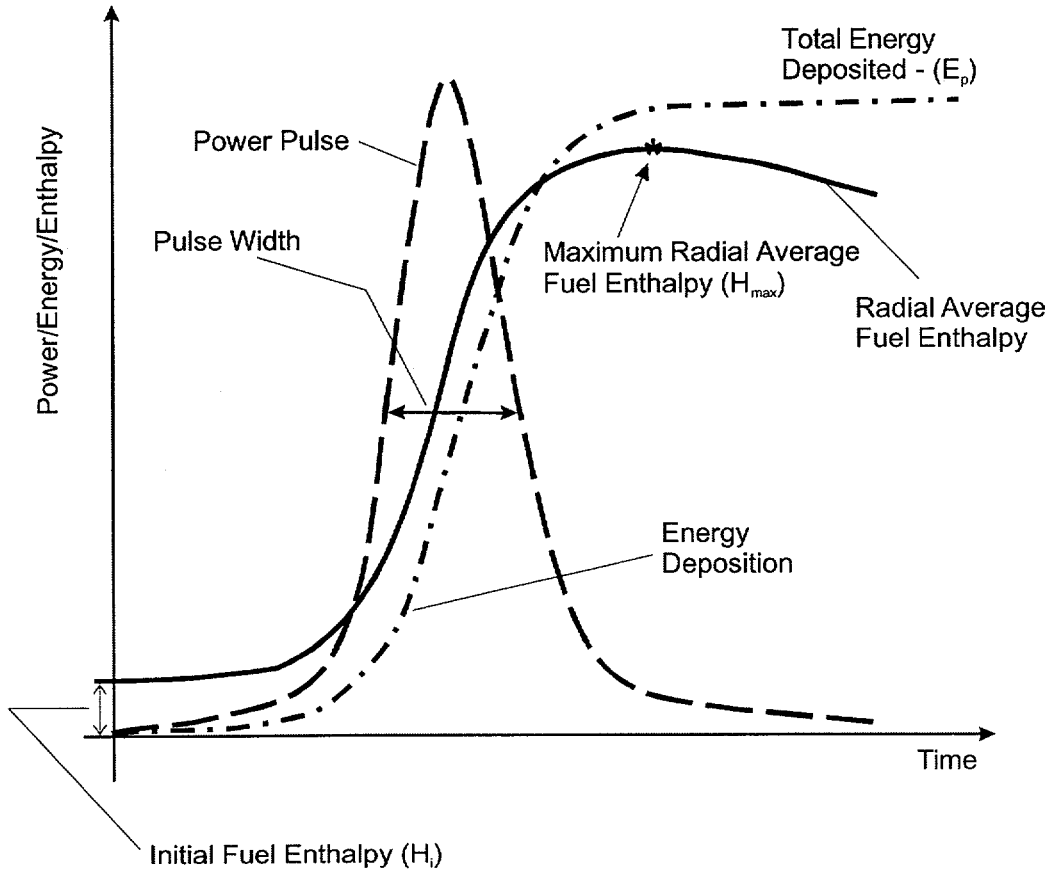

Figure 2-1
RIA power pulse schematic showing the relationship between power, energy deposition, and radial average peak fuel enthalpy.

Table 2-1
CABRI REP Na Test Rods
[Schmitz and Papin 1998; MacLachlan 2000a; MacLachlan 2000b]

Test	Peak Pellet Burnup (GWd/tU)	Oxide Layer (microns)	Fuel Type	Pulse Width (msec)	Max. H (cal/gm)	H at Failure (cal/gm)	Fuel Dispersal
Na-1	65	>80 – spall	17x17	9.5	115	30	Yes
Na-2	33	10	17x17	9.5	220		
Na-3	52	50	17x17	9.5	138		
Na-4	62	85	17x17	70	81		
Na-5	64	20	17x17	9.1	113		
Na-6	47	35	17x17 – Mox	35	138		
Na-7	55	50	17x17 – Mox	40	140	120	Yes
Na-8	60	130 - spall	17x17	78	105	83	No
Na-9	28	10	17x17 – Mox	34	203		
Na-10	64	>80 - spall	17x17	31	112	79	No
Na-11	64	~20	17x17 - M5	35	105		
Na12	65	~80	17x17 - Mox	65	~90		

Table 2-2
NSRR PWR Test Rods [Fujishiro 1992; Fuketa 1996; Fuketa 1997; Fuketa 1998; Fuketa 2000]

Test	Burnup (GWd/tU)	Oxide Layer (microns)	Fuel Type	Pulse Width (msec)	Max. H (cal/gm)	H at Failure (cal/gm)	Fuel Dispersal
HBO-1	50	40-50	17x17	4.4	73	60	Yes
HBO-2	50	30-40	17x17	6.9	37		
HBO-3	50	22	17x17	4.4	74		
HBO-4	50	18	17x17	5.4	50		
HBO-5	44	35-60	17x17	4.4	80	77	Yes
HBO-6	49	20-30	17x17	4.4	88		
HBO-7	49	30-50	17x17	4.4	88		
MH-1	39	5	14x14	5.3	47		
MH-2	39	5	14x14	5.0	55		
MH-3	39	5	14x14	4.8	67		
GK-1	42	10	14x14	4.8	93		
GK-2	42	10	14x14	4.8	90		
OI-1	39	N/A	17x17	4.4	106		
OI-2	39	N/A	17x17	4.4	108		
TK-1	38	7	17x17	4.4	125		
TK-2	48	15-35	17x17	4.4	107	60	Yes
TK-3	50	8	17x17	4.4	99		
TK-4	50	20	17x17	4.4	98		
TK-5	48	25	17x17	4.4	101		
TK-6	38	15	17x17	4.4	125		
TK-7	50	15-35	17x17	4.4	95	86	Yes

Table 2-3
NSRR BWR Test Rods [Nakamura 1994; Fuketa 2000]

Test	Burnup (GWd/tU)	Oxide Layer (microns)	Fuel Type	Pulse Width (msec)	Max. H (cal/gm)	H at Failure (cal/gm)	Fuel Dispersal
TS-1	26	6	7x7	6.7	55		
TS-2	26	6	7x7	6.2	66		
TS-3	26	6	7x7	5.6	88		
TS-4	26	6	7x7	5.0	84		
TS-5	26	6	7x7	4.5	98		
FK-1	45	11	8x8BJ	4.4	130		
FK-2	45	11	8x8BJ	5.3	70		
FK-3	41	15	8x8BJ	4.4	145		
FK-4	56	10	8x8	4.4	140		
FK-5	56	10	8x8	5.3	70		
FK-6	61	20	8x8	4.3	131	70	Yes
FK-7	61	20	8x8	4.3	129	62	Yes
FK-8	61	20	8x8	7.3	65		
FK-9	61	20	8x8	5.7	93	86	No

Table 2-4
IGR/BIGR Irradiated VVER Test Rods (Water 20°C and 0.1 MPa) [Yegorova 1999; Bibilashvili et al. 2000]

Test	Burnup (GWd/tU)	Oxide Layer (microns)	Fuel Type	Pulse Width (msec)	Max. H (cal/gm)	H at Failure (cal/gm)	Fuel Dispersal
H1T	48	5	1000	800	151		
H2T	48	5	1000	800	213	213	No
H3T	48	5	1000	800	252	252	No
H4T	48	5	1000	800	114		
H5T	48	5	1000	800	176	176	No
H6T	48	5	1000	800	87		
H7T	48	5	1000	800	187	187	No
H8T	48	5	1000	800	61		
BIGR-1	48	5	1000	3	142		
BIGR-2	48	5	1000	3	115		
BIGR-3	48	5	1000	3	138		
BIGR-4	61	5	440	3	125		
BIGR-5	48	5	1000	3	146		
BIGR-6	48	5	1000	3	153		

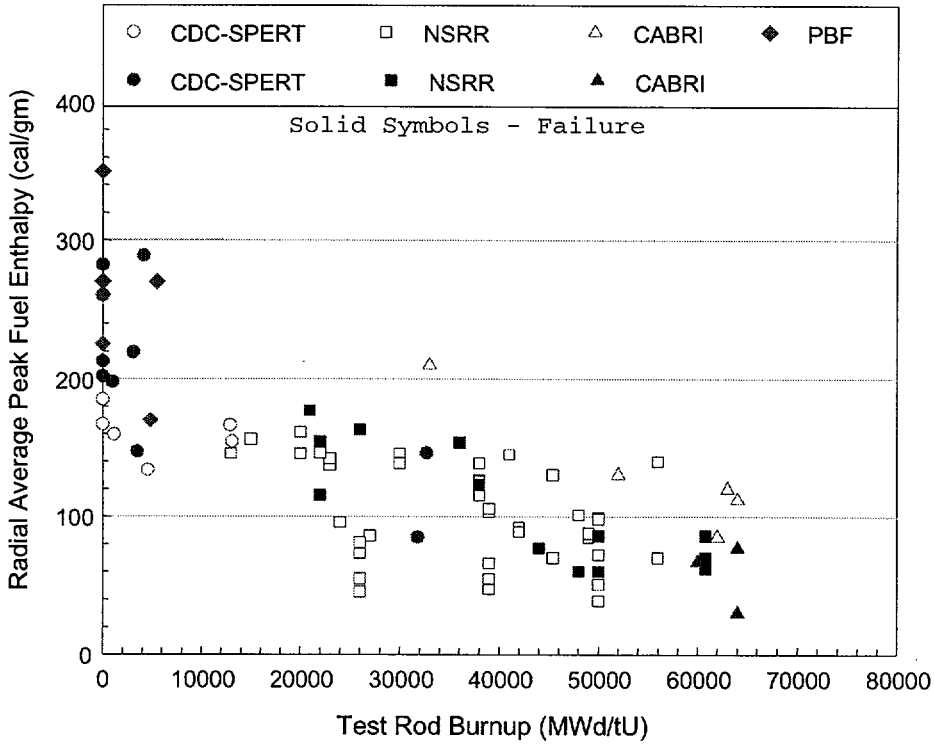

Figure 2-2
The radial average peak fuel enthalpy as a function of test rod burnup for RIA-simulation tests performed in the US, France, and Japan. Tests with cladding failure are indicated by solid symbols. The downward trend in the data is caused by the decrease in test rod reactivity with burnup accumulation.

2.2.1 CABRI REP Na Program

A review of the CABRI REP Na program on PWR fuel rods with non-spalled oxide layers at burnup levels up to 64 GWd/tU (see Appendix A for definition of oxide spallation) finds that these rods survived the RIA tests with minimum of consequences. The only tests on UO_2 fuel that experienced cladding failure in the CABRI REP Na program were Na-1, Na-8 and Na-10, which contained cladding with spalled outer surface oxide layers. Accompanying the spalled oxide layers in these tests were localized hydrides up to 50% of the cladding wall thickness, identified by neutron radiography and post-test metallography. Recent tests REP Na-8 and REP Na-10 failed at fuel enthalpy levels around 60 cal/gm and each rod had an additional energy deposition of ~30 cal/gm following cladding failure. Although these test rods contained extensive cladding spallation and hydride localization, only trace amounts of volatile fission products were released into the coolant, no fuel dispersal was experienced, and massive loss of cladding integrity was not observed even though an additional ~30 cal/gm was deposited after cladding failure. CABRI REP Na-8 and Na-10 further support the concept that loss of cladding ductility by formation of localized hydrides is the major cause of cladding failure during rapid

energy deposition events at elevated temperatures. Each of these tests exhibited brittle cladding cracks associated with localized hydrides.

The root cause of the low enthalpy failure of CABRI REP Na-1 continues to be unresolved. As a result, the International CABRI Water Loop Project has formed a special REP Na-1 Task Force with the objective of reaching a general consensus on the cause of cladding failure for this test. Members of the REP Na-1 Task Force have initially focused on the hypothesis of failure proposed by H. Chung at the recent ANS LWR Fuel Performance Topical Meeting [Chung 2000]. Chung has raised a concern that the pre-test initial conditions may have influenced the hydride morphology within the cladding and produced significant Zr-4 embrittlement. This embrittlement may then have influenced the fracture behavior of the cladding during the power deposition. The REP Na-1 Task Force has also reviewed the detection of the initial failure by the in-pile microphones to determine the reliability of the time of failure. The response of other in-pile measurements, such as the sodium flow rate and the pressure transducer response are being compared to the microphone data to confirm the time of cladding failure. However, it is the opinion of most members of the task force that REP Na-1 is an outlier test that need not be considered in the evaluation of high burnup fuel behavior during an RIA.

The results from the CABRI tests on MOX fuel irradiated between 28 and 47 GWd/tU show higher fission gas release and an increased PCMI loading from fission gas-induced pellet swelling [Schmitz and Papin 1999]. CABRI REP Na-7, which had a burnup of 55 GWd/tU, failed during the power pulse although the cladding corrosion layer was less than 50 microns [Schmitz and Papin 1999]. The Na-7 results suggest that a significant contribution of fission gas expansion or pressure loading was applied to the cladding during the power pulse to cause cladding failure.

2.2.2 NSRR Program

Since the mid-nineties, several additional RIA-simulation tests on PWR and BWR test rods have been performed in the NSRR facility. For PWR rods, an additional three tests have been conducted on the high-tin (~1.5% Sn) cladding material in the HBO series and a total of seven tests on low-tin (~1.3% Sn) cladding material have been conducted in the TK series. The burnup range for the test rods was between 38 and 50 GWd/tU. The NSRR facility has also conducted a total of nine tests on BWR rods refabricated from fuel rods previously irradiated in the Fukushima plant to a burnup range between 45 and 61 GWd/tU.

Evaluation of the PCMI-related failures in the PWR test rods HBO-1, HBO-5, TK-2 and TK-7 shows a correlation between the cladding outer oxide thickness and the potential for cladding failure. A plot of the peak fuel enthalpy versus the outer surface oxide layer thickness is shown in Figure 2-3. A failure boundary that has an oxide layer thickness dependency is indicated in the data. The curve shown in Figure 2-3 is just an engineering approximation. A more in-depth review of this data suggests that the cladding failure response in the NSRR tests is related to the hydride rim thickness. Post-test examinations on unfailed tests HBO-6 and HBO-7 found part-wall microcracks in the outer surface oxide and hydride rim layer that were blunted in the ductile Zircaloy substrate [Fuketa et al.1996]. Similar microcracks were also observed in the failed tests HBO-1 and HBO-5 in the vicinity of the through-wall cracks. The low initial cladding

temperature and the narrow pulse width in the NSRR tests magnify the influence of the hydride rim at the cladding outer surface on the effective cladding ductility.

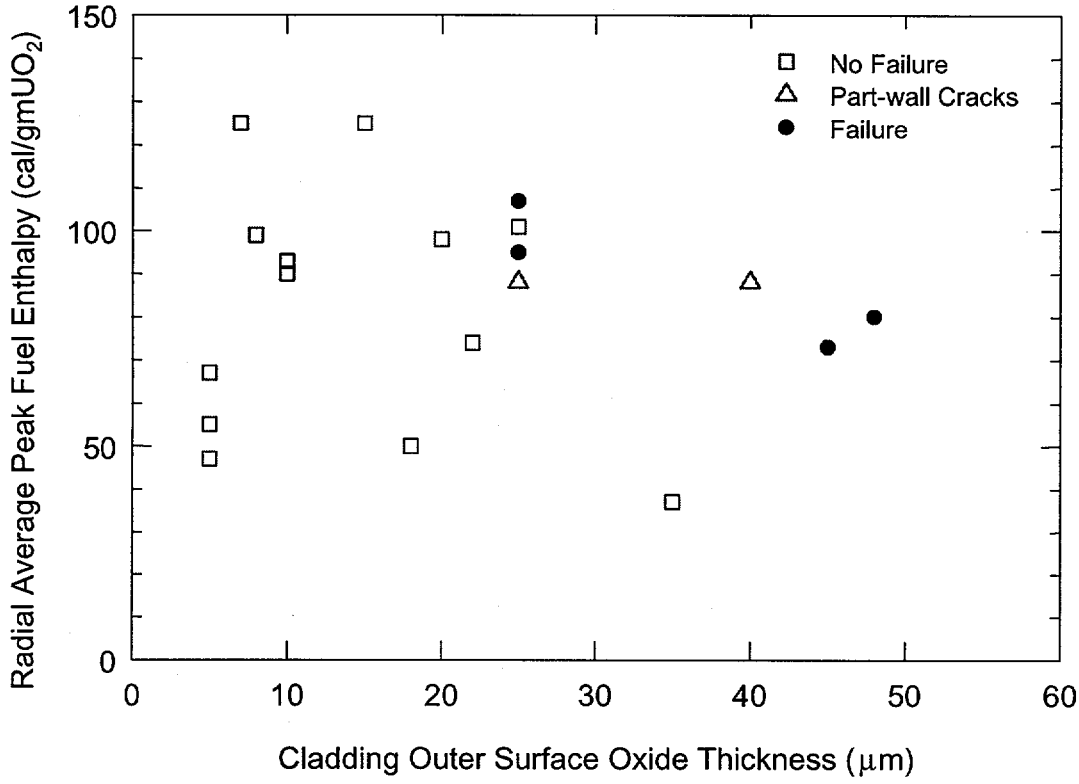

Figure 2-3
Peak Fuel Enthalpy versus Oxide Thickness from the NSRR Experiments

RIA-simulation tests using BWR rods have been performed on test rods refabricated from 8x8 zirconium liner cladding fuel rods irradiated to 61 GWd/tU. As shown in Table 2-3, no BWR test rods have failed below a burnup level of 56 GWd/tU up to peak fuel enthalpy levels of 140 cal/gm. A review of the tests finds no unusual behavior exhibited by the BWR test rods. The permanent cladding hoop strains are below 2% and the transient fission gas release is below 20%. This level of cladding strain is consistent with pellet thermal expansion during the energy deposition and does not indicate any enhancement of the PCMI loading from burnup-induced gaseous swelling or expansion. Compared to the PWR tests, these results are lower than the HBO and TK series. Recently, four tests have been performed on BWR rods at a burnup of 61 GWd/tU. Pre-test examinations show extensive fuel-clad bonding and almost complete gap closure. Tests FK-6 and FK-7 were tested to 130 cal/gm peak fuel enthalpy and each one failed between 60 and 70 cal/gm, broke into several pieces and dispersed finely fragmented fuel pellets into the coolant. FK-8 was tested with a wider pulse to peak fuel enthalpy of 65 cal/gm without cladding failure. Cladding failure may have been avoided in FK-8 because the wider pulse produces higher cladding temperature and thus, an increase in the cladding ductility. FK-9 also

included a wider pulse, but was tested to a peak fuel enthalpy of 90 cal/gm. Cladding failure was observed at 86 cal/gm from in-pile instrumentation. These results are still under investigation.

The test conditions (low initial coolant temperature and narrow pulse width) used thus far in the NSRR tests produce high cladding stress prior to any significant cladding heating by heat conduction from the pellet. At low temperature, the effective ductility of Zircaloy cladding containing non-uniform hydride layers is low and may be insufficient to accommodate fuel pellet expansion. The results obtained from tests conducted in the NSRR facility highlight the influence of the initial cladding temperature and the pulse width on the cladding failure response. Because these tests are conducted under room temperature coolant conditions, the test results are not representative of the fuel rod response for a HZP RIA event. Furthermore, these results require analytical evaluation to allow for comparison to other test programs, such as CABRI, and to assess the key mechanisms in the fuel rod response during an RIA event.

In the majority of the NSRR tests that resulted in cladding failure, a small amount of fuel dispersal was observed following cladding failure [Fuketa et al.1998]. The presence of fuel dispersal in the NSRR tests is related to the narrow pulse widths used in the RIA simulations. Since almost no heat conduction occurs during the energy deposition in NSRR, the pellet is under a large compressive stress state, particularly in the rim region. Upon cladding failure, the sudden removal of the confinement stress within the fuel produces local cracking and expulsion of small particles through the crack opening. The relevance of the NSRR tests with fuel particle dispersal will be discussed in more detail in Section 4.1.2.

2.2.3 IGR/BIGR Program

The IGR/BIGR program was performed in Russia to evaluate the failure mechanisms and failure thresholds for VVER fuel rods during RIA conditions [Asmolov 1996, Yegorova 1999, Bibilashvili 2000]. The program included approximately 200 tests on unirradiated VVER test rods and 14 tests on VVER test rods with burnup levels in the range of 50 GWd/tU to provide information on the effects of energy deposition, pulse width, initial rod internal pressure, and temperature. The VVER test rods differ from those tested in the French and Japanese programs in two ways: the use of Zr-1%Nb cladding material and the presence of a central hole in the fuel column. The IGR/BIGR test conditions are similar to those used in the NSRR test program and included three different coolant conditions: water at 20°C and atmospheric pressure, air at 20°C and atmospheric pressure, and water at 20°C and 16 MPa pressure.

The mode of cladding failure for the tests on VVER rods was shown to depend on the pressure differential across the cladding. For tests with a positive pressure differential (prepressurized 1.5 MPa above the coolant pressure), the dominant fuel rod failure mechanism was high temperature ductile rupture (clad ballooning) and the cladding survived the lower temperature PCMI during the power pulse. The high cladding temperatures required to produce ballooning were a result of departure from nucleate boiling (DNB) that occurred either during the latter portion of the power pulse or after the completion of the power pulse. From analytical calculations, estimated peak cladding temperatures exceeded 1300 K in the high energy tests. For tests with a negative or zero pressure differential (prepressurization at or below coolant pressure), cladding failure was by melting due to interaction with molten UO_2 material.

The peak fuel enthalpy at failure depends on the initial conditions of the tests and is listed in Table 2-4.

Table 2-5
Summary of RIA-Simulation Tests on VVER Fuel in the IGR/GIRDA/BIGR Reactors

Type/Number of Tests	P_{rod} (MPa)	$P_{coolant}$ (MPa)	Pulse Widths (msec)	Radial Average Peak Fuel Enthaply (cal/gm)	Failure Threshold (cal/gm)
Unirradiated Unpressurized Rods (40)	0.1	0.1	2.75 - 1000	130 - 320	260 - 290
Unirradiated Pressurized Rods (129)	1.6 - 2.5	0.1	1.8 - 1000	20 - 500	160 - 180
Unirradiated Pressurized Rods (8)	2.5	16	440 - 600	175 - 250	250
Irradiated Pressurized Rods (14)	1.7	0.1	3 - 800	61 - 252	160 - 170

Almost no difference was observed between the failure response of the unirradiated and irradiated test rods to a burnup level near 50 GWd/tU because the Zr-1%Nb cladding material retains a significant amount of ductility at high burnup due to lower corrosion and less hydrogen absorption. As a consequence, the cladding can accommodate the PCMI loading during the energy deposition and prior to DNB. A comparison of the unirradiated and irradiated pre-pressurized tests performed in the IGR/BIGR test program with earlier tests performed in NSRR on pre-pressurized rods is shown in Figure 2-4. As can be seen, no large differences are observed between the failure threshold derived from the NSRR program using Zr-4 cladding and the IGR/BIGR program using Zr-1%Nb cladding. These results indicate that the high temperature failure response during an RIA event is the same for the two cladding types. Furthermore, these results demonstrate that the maximum fuel enthalpy at failure is primarily a function of positive pressure differential across the cladding. The cladding failure mode changes from a melt response to ballooning/rupture above a positive pressure differential of 1 MPa.

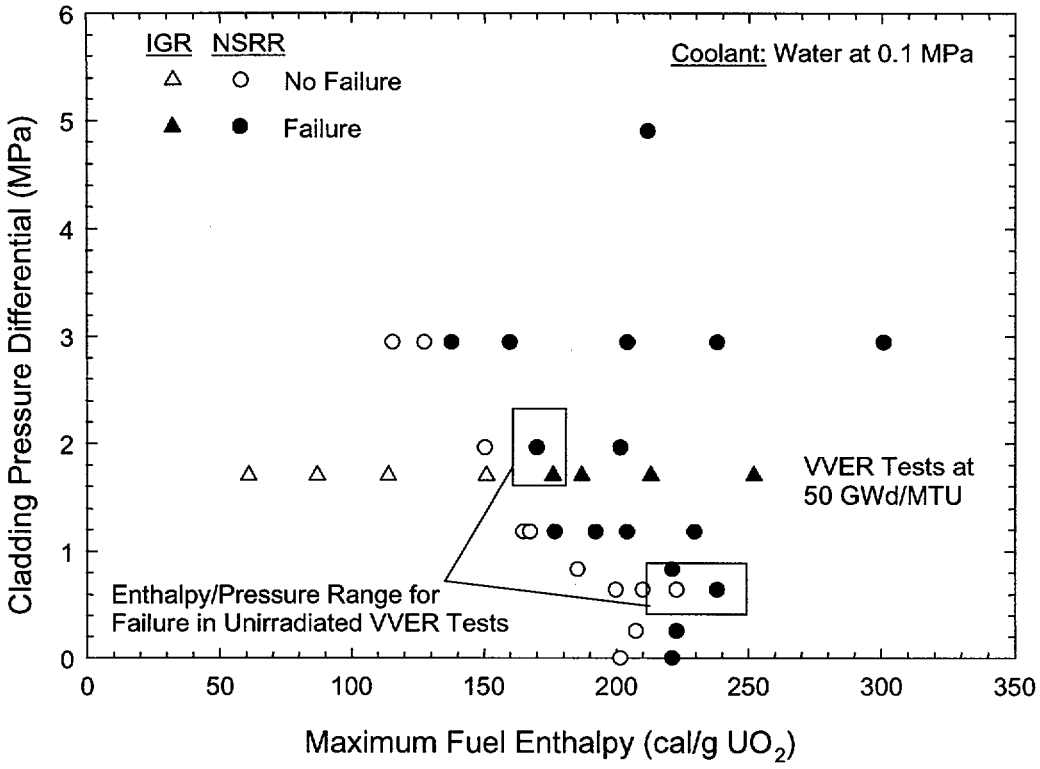

Figure 2-4
Initial Internal Pressure versus Energy Deposition for the NSRR and IGR/BIGR Tests

2.2.4 Summary

In tests conducted in NSRR and CABRI above 55 GWd/tU, the effect of burnup has been shown to increase the PCMI forces on the cladding by the gradual reduction of the fuel-cladding gap thickness during steady state irradiation. The CABRI REP Na-4, REP Na-5 and REP Na-11 tests at 60+ GWd/tU and the recent NSRR tests FK-4 and FK-5 at 56 GWd/tU did not fail after experiencing maximum fuel enthalpy increases between 70 and 140 cal/gm. These test rods had cladding material with sufficient ductility to accommodate the PCMI loading strains. The results from these tests demonstrate that the main load imposed on the cladding is from PCMI mechanisms caused by pellet thermal expansion combined with burnup related processes. The role of fission gas-induced transient swelling is much less for UO_2 fuel rods at the burnup and temperature conditions experienced by the tests.

The results from RIA-simulation tests on VVER rods at burnup levels near 50 GWd/tU demonstrate that the zirconium-niobium alloy cladding will survive the PCMI phase without failure. The primary failure mode is by high temperature processes that occur once heat conduction is initiated. For test rods with an internal pressure that exceeded the external pressure, ballooning and burst failure of the cladding was initiated at energy levels that produced cladding temperatures above 1200 K. Since the irradiated VVER fuel rod designs contain a central hole, the larger gas volume and the rapid axial gas communication was able to support

the clad ballooning deformations that led to failure. The tests on VVER fuel overestimate the impact of gas pressure on ballooning for high burnup LWR fuel rods, which have restricted axial gas communication due to gap closure and pellet-clad bonding. The cladding temperature at failure increases, as well as the peak fuel enthalpy, for low or negative pressure drops across the cladding. These results are consistent with similar tests conducted in NSRR during the 1970's.

In development of a failure threshold from all the data shown in Figure 2-2, the statistical failure/no failure method used to evaluate the data produces mixed results because of factors introduced during irradiation such as the decrease in fuel rod reactivity and the decrease in cladding ductility with fluence and corrosion for older cladding designs. In addition, variations in test conditions make it difficult to directly compare the results from different test programs. To more fully understand the contribution of burnup, cladding embrittlement and test conditions requires analysis of the test rods using sophisticated analytical capabilities coupled with data from separate effects tests to distinguish between the various effects. Through such an approach, the circumstances leading to fuel rod failure can be determined considering the parameters that influence the response of the fuel and cladding.

2.3 Separate Effects Tests

An important element in the evaluation and modeling of fuel behavior during an RIA event are the data from separate effects tests. The main separate effects tests used in the modeling and analysis of RIA-simulation experiments are the mechanical property tests on irradiated cladding material. The data obtained from cladding mechanical property tests and the method employed to utilize this data with the analytical methods for RIA-simulation experiments are described below.

2.3.1 Cladding Mechanical Properties Database

Data describing the effects of operation on the cladding material tensile strength and elongation are necessary to understand the behavior of irradiated test specimens during RIA-simulation tests and to evaluate the performance of irradiated fuel during a hypothetical RIA event. Similar data is also required to demonstrate adequate cladding performance during normal operation and anticipated operational occurrences. As a result, several post-irradiation test programs have been conducted to evaluate the effects of irradiation on the cladding mechanical properties. The outcome of such test programs has been to highlight the changes in cladding mechanical properties caused by fast neutron damage, absorption of hydrogen from the corrosion process, and temperature. An example of the mechanical tests used and results obtained for irradiated Zircaloy cladding is presented by Garde [Garde 1989].

Table 2-5 lists the mechanical property test programs used as part of the industry assessment of RIA fuel behavior to develop the strength, elongation and critical strain energy density relationships for irradiated Zircaloy cladding [Papazoglou and Davis 1983; Balfour et al. 1985; Newman 1986; Smith et al. 1994a; Smith et al. 1994b; Lemoine and Balourdet 1997; Hermann et al. 2000; Kuo et al. 2000]. The cladding material used in these test programs includes different cladding designs, e.g. 14x14 and 17x17, irradiation conditions, oxide layer thickness levels, and

zirconium hydride distributions. The programs summarized in Table 2-5 include most of the mechanical property tests conducted on high burnup Zircaloy-4 cladding material. As indicated, test results are included from samples that contained cladding outer surface oxide layers with cracking, flaking, and spallation.

In general, three types of mechanical property tests are used in the programs listed in Table 2-5: uniaxial tube tension tests, uniaxial ring tension tests, and biaxial tube burst tests. Uniaxial tube tension tests consist of tube samples approximately 125 mm long, with a central gauge section of ~50 mm. These specimens are tested by loading in the axial direction at strain rates of ~$5x10^{-5}$/sec in most cases. Uniaxial ring tension tests consist of a thin ring sample fabricated to widths between 2.5 and 7 mm and with or without a machined gauge section. Typical machined gauge sections are ~3 mm long and 1.5 mm wide. For specimen designs without a machined gauge section, the experimenters assumed that the gauge length was 20% of the mid-wall circumference in the calculation of the hoop strain [Garde et al. 1996]. The ring tension specimens are tested with special inserts to provide loading in the hoop direction. For uniaxial tube tension and ring tension samples obtained from fuel rods, the pellet material is removed by drilling and chemical etching. Biaxial tube burst tests are performed on 200 mm long tube samples using some type of hydraulic fluid to pressurize the sample. The pellet material is either completely or partially removed prior to testing. Closed-end burst tests are performed in most cases. The mechanical properties determined from the three different test types include yield stress, ultimate tensile stress, uniform elongation and total elongation.

2.3.1.1 Influence of Irradiation on Cladding Mechanical Properties

A review of the mechanical properties measured for irradiated cladding at burnup levels greater than 50 GWd/tU indicates that the effects of fast neutron damage (irradiation hardening) causes only an incremental increase from low burnup values in the yield stress and ultimate tensile stress. Saturation of the yield and ultimate tensile strength with fast neutron damage occurs below fluence values of 3-4x10^{21} n/cm^2 (E > 1 MeV). The effect of fluence on the yield stress of CWSR Zircaloy-4 material is shown in Figure 2-5 for uniaxial tension tests. Similar results are obtained from burst specimens.

The uniform and total elongation values decrease with accumulation of fast neutron damage. The most significant reduction in uniform and total elongation occurs during the first cycle of operation at fast fluence levels approaching 3 to 4x10^{21} n/cm^2 (E > 1 MeV). After the first cycle of irradiation, the uniform elongation value for Zircaloy-4 SRA material is reduced from 4 to 5 % for unirradiated material down to values between 1 and 3% for irradiated material. The reduction of the uniform elongation is observed in all of the different mechanical property test methods. Similarly, the total elongation decreases from 20 to 30% for unirradiated material to values between 10 and 15% after 1 cycle of operation. The extent of the reduction depends somewhat on the type of mechanical property test (uniaxial or biaxial) and the susceptibility of test sample to develop bending within the gauge section. Beyond this level of fast fluence, the uniform and total elongation remain about constant until a fast fluence of 9x10^{21} n/cm^2 (E > 1 MeV).

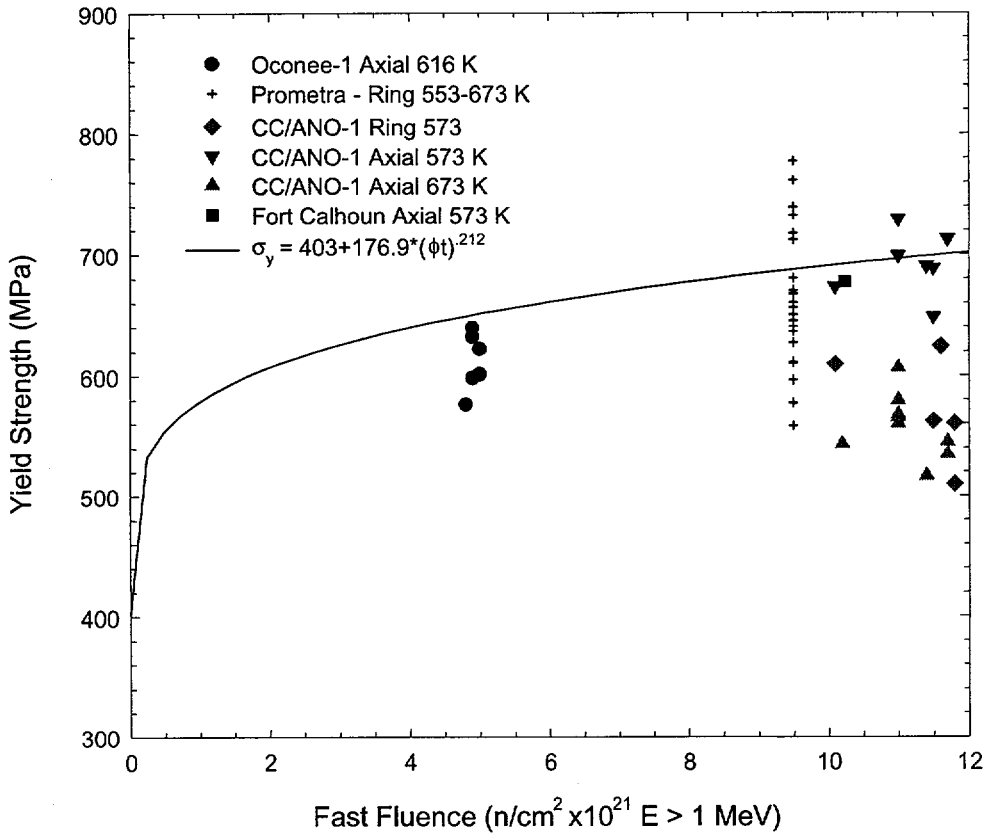

Figure 2-5
Cladding yield stress as a function of fast neutron fluence. Irradiation hardening saturates at fast fluence levels above 3x10^{21} n/cm^2 (E>1 MeV).

At the fluence levels corresponding to extended burnup ($\phi t > 9x10^{21}$ n/cm^2 E> 1 MeV), the concentration of zirconium hydrides and the zirconium hydride distribution in the cladding can further influence the cladding mechanical properties. Mechanical tests on cladding with hydrogen levels above 300 ppm begin to exhibit the effects of hydride precipitates on both the uniform and total elongation. The uniform elongation can be reduced below 1% and the total elongation can decrease to below 2% for biaxial burst tests.

Figure 2-6 contains the total plastic elongation measurements from axial tension, ring tension, and tube burst tests conducted on cladding material irradiated to fast fluence levels between 9 and 12x10^{21} n/cm^2 (E > 1 MeV). The current evaluation uses the oxide thickness to depict the influence of hydrides on the cladding mechanical properties. This approach was necessary because the methods employed to determine the hydrogen content for a given test sample were not consistent between the various test programs. Since the hydrogen within the cladding comes from the corrosion process, the oxide thickness can be assumed to represent the average hydrogen content within the cladding. Finally, the oxide thickness was normalized using the cladding wall thickness to account for the variation in cladding designs, i.e., 17x17 and 14x14.

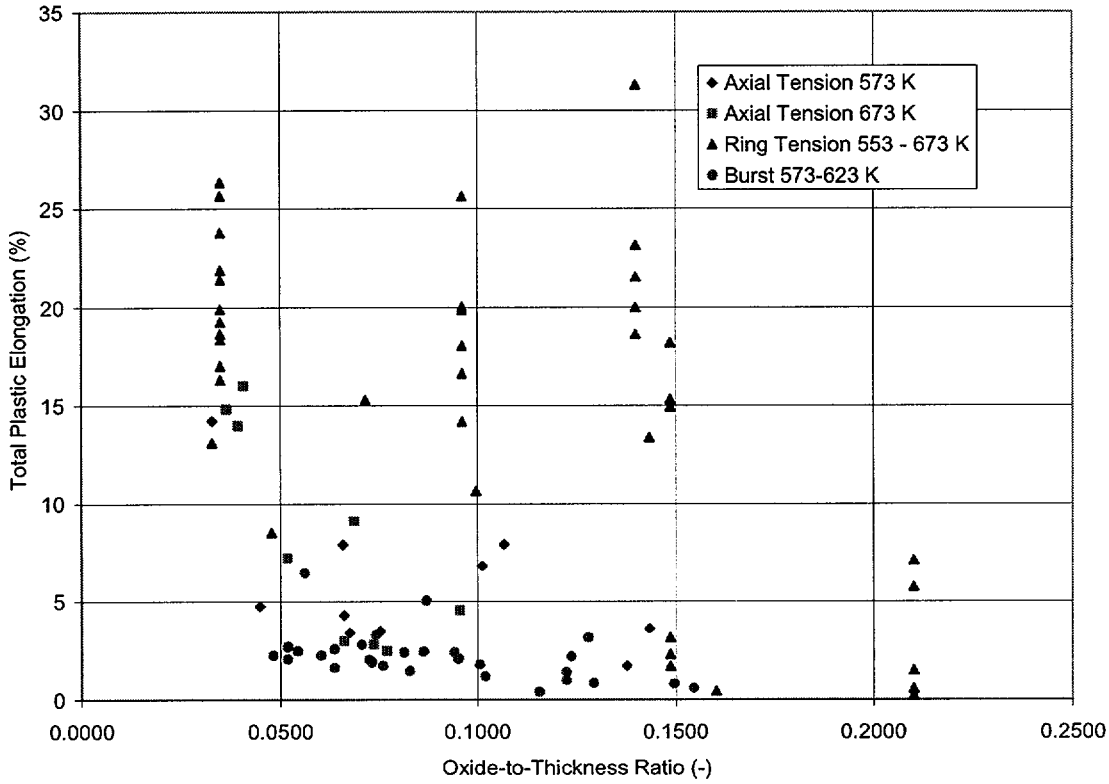

Figure 2-6
Total plastic elongation as a function of oxide-to-thickness ratio. Data obtained from uniaxial ring tension, uniaxial axial tension and burst tests on irradiated cladding at fluence levels above $9x10^{21}$ n/cm^2 (E > 1 MeV).

The total plastic elongation decreases as a function of the outer surface oxide thickness. Although only limited data is available, the effect of hydrogen is more pronounced in the axial tension data. The data shown in Figure 2-6 indicate that both the ring tension and the burst total plastic elongation data are independent of the hydrides in the cladding below oxide thickness-to-cladding thickness ratios of 0.1 to 0.12 at temperatures above 573 K. Above this oxide thickness, the potential to form localized hydrides increases and the total plastic elongation values begin to drop below 1% for samples with localized hydrides. Those test samples that came from rods with localized hydrides or were confirmed to have localized hydrides within the samples are indicated in Figure 2-6. The uniform plastic elongation data shown in Figure 2-7 also decreases as a function of outer surface oxide thickness. The influence of oxide thickness is observed in both the uniaxial and biaxial tests. Uniform plastic elongation values that are below 0.5% are associated with cladding with localized hydrides as indicated in Figure 2-7.

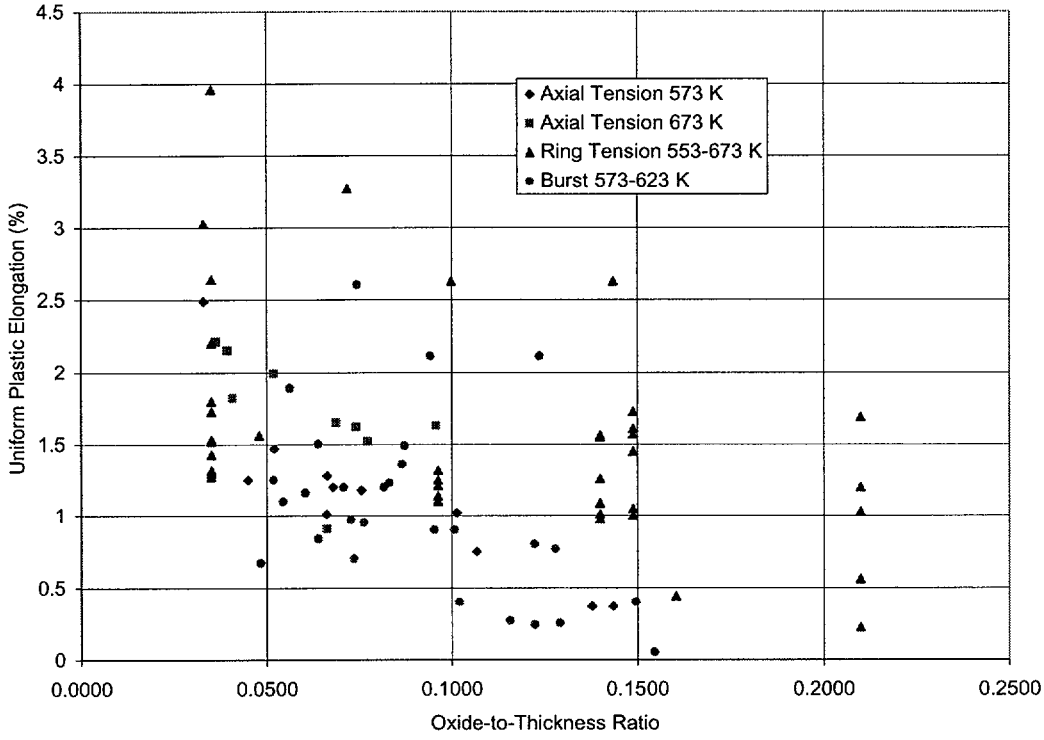

Figure 2-7
Uniform plastic elongation as a function of oxide-to-thickness ratio. Data obtained from uniaxial ring tension, uniaxial axial tension and burst tests on irradiated cladding at fluence levels above $9x10^{21}$ n/cm^2 (E > 1 MeV).

As shown in Figures 2-6 and 2-7, non-uniform zirconium hydride distributions corresponding to high hydrogen concentrations (> 700 ppm) can reduce the uniform and total plastic elongation, as well as, the ultimate tensile strength. Garde, et al. presented results on uniform and total plastic elongation measurements from cladding with localized hydride regions [Garde et al. 1996]. These data show that the cladding total plastic elongation can decrease to below 1% for cladding average hydride volume fractions above 80% in the vicinity of the fracture location. Formation of localized hydride accumulations leading to 80% volume fraction requires the migration of hydrogen under thermal gradients. Non-uniform oxide layers as a consequence of outer surface oxide spallation can cause the thermal gradients sufficient to promote hydrogen migration, depending on such factors as the oxide layer thickness and operating power level. Oxide spallation is addressed in Appendix B.

2.3.1.2 Sources of Data Scatter

The mechanical property data for irradiated cladding obtained from the different test methods contains a certain level of data scatter that is caused by two main sources. First, the testing methods introduce data scatter by such factors as specimen design and fabrication, loading and heating conditions, and measurement uncertainties. Second, material variability arising from

differences in initial cladding material fabrication (composition and heat treatment), cladding geometry (wall thickness and outer diameter), irradiation temperature, and hydrogen concentration also contribute to the scatter in the measured material strength and elongation values. An understanding of the sources of data scatter is important in the development of mechanical property dependencies on fast fluence, hydrogen content, and temperature.

The mechanical properties of irradiated cladding are measured using testing methods that inherently introduce some amount of data scatter. Developing a uniaxial test specimen from clad tubing is difficult and the specimen designs deviate from traditional uniaxial tension specimens. As a result, two main problems arise in the ring tension and axial tension tests. For the ring tension, the double-D loading method can introduce bending within the gauge section. The amount of bending is a function of the tolerances between the loading inserts and the sample and can affect the measured elongation values. Also, the gauge section in both the ring tension and axial tension test specimens is not well defined. This also can introduce uncertainties in the total elongation strains measured in the post-test examinations. Efforts are underway in the NRC-sponsored programs at ANL to improve the test specimens to eliminate bending and improve the strain measurements [Daum et al. 2001; Link et al. 1998]. However, the data scatter arising from the testing methods must be recognized to always be present in the data.

The condition or material characteristics of the cladding sample being tested also influence the measured mechanical properties of irradiated cladding. Variability in fabrication processes can influence the impurity content and/or the heat treatment of the cladding. Mechanical properties of cladding from different fuel vendors will always display some variability for unirradiated material. Irradiation further complicates the cladding mechanical properties because irradiation damage accumulation is influenced by the operating temperature of the cladding [Rowland 1984; Lyon et al. 2001]. Therefore, samples removed from the upper regions of the rod can have different irradiation hardening characteristics compared to the lower region of the rod because of the higher cladding temperature. These uncertainties are also inherent to the data and are difficult to account for in any modeling activity.

Because of the nature of irradiated cladding, data scatter will always be present in the mechanical properties reported. This must be recognized when developing material models for irradiated Zircaloy material.

Table 2-6
Mechanical Property Tests

Program	Fuel Type	Max. Bu (GWd/tU)	Max. Fast Fluence (n/cm^2)	Range of Oxide Thickness (μm)	Temperature Range (K)	Strain Rate (/sec)
ESEERCO Hot Cell Program on Zion Rods						
Burst	15x15	49	$9.4x10^{21}$	15 - 25	588	$2x10^{-5}$
ABBCE-DOE Hot Cell Program on Fort Calhoun Rods						
Burst	14x14	53	$8x10^{21}$	30 - 50	588	$6.7x10^{-5}$
EPRI-B&W Hot Cell Program on Oconee-1 Rods						
Axial Tension	15x15	25	$5x10^{21}$	< 20	616	$8x10^{-5}$
Ring Tension						
Burst						
EPRI-ABBCE Hot Cell Program on Calvert Cliffs-1 Rods						
Axial Tension	14x14	68	$12x10^{21}$	24 - 110‡	313 - 673	$4x10^{-5}$
Ring Tension				24 - 115‡	573	$4x10^{-5}$
Burst				36 - 110‡	588	$6.7x10^{-5}$
ABBCE-DOE Hot Cell Program on ANO-2 Rods						
Axial Tension	16x16	58	$12x10^{21}$	24 - 46	313 - 673	$4x10^{-5}$
Burst				24 - 46	588	$7x10^{-5}$
EdF-IPSN PROMETRA Program						
Ring Tension	17x17	63	$10x10^{21}$	20 - 120‡	298 - 673	.01 - 5
Nuclear Fuel Industry Research Program-III						
Burst	15x15	51	$9x10^{21}$	40 - 110‡	573 - 623	$5x10^{-5}$

‡- Several samples were obtained from cladding with spalled oxide layers.

2.3.2 Cladding Integrity Model

A first approach to develop an integrity model for high burnup cladding subjected to an RIA event might be to use a simple strain-to-failure (ductility limit) criterion. This strain-to-failure criterion would be measured directly in a mechanical property test and can be a function of temperature, hydrogen content, strain rate etc. Unfortunately, however, strain is not a path independent response quantity and, consequently, does not uniquely characterize a failure state of the material; further, it depends on the rate of loading and the multi-axial condition of the imposed stresses. A practical difficulty in using a strain limit is the choice between the "uniform elongation" and the "total elongation". The latter is a uniaxial limit state that is subject to the restrictions outlined above, but the former is an apparent limit state that has significance only in describing the stress-strain test and plays no role in modeling and analysis. The uniform elongation is the strain at the point of maximum load in an engineering-stress-engineering-strain curve, and is assumed to be the onset of plastic instability. Thus, when the source of loading is purely pressure, it is often argued that the uniform elongation becomes the true failure measure. By contrast, PCMI is a displacement controlled loading, and thus could not be judged by such a strain measure. More importantly, the true-stress-true-strain curve is the material property relation used in RIA modeling and analysis where the calculated strain response is a single quantity with no possible way of identifying a uniform-elongation strain. It would seem, then, that the use of a strain criterion as a failure measure for judging RIA events is unworkable.

A stress-based criterion suffers from similar deficiencies, in that it does not recognize the state of deformations and does not distinguish between a load-controlled (pressure type) and a displacement controlled (PCMI type) loading events. Consequently, neither the strain state alone nor the stress state alone is sufficient to describe a failure state. The appropriate approach, then, is to develop a failure criterion that combines both the stress and the strain states, for which the strain energy density concept is best suited. The material resistance would be judged in terms of a critical value of the strain energy density (CSED), and the applied loading would be described in the calculated response in terms of the strain energy density (SED). The CSED is determined from material property tests as function of temperature, fast fluence, hydrogen content and other material conditions. The SED represents the accumulation of the total mechanical energy during mechanical loading of the cladding during an RIA event.

2.3.2.1 Theoretical Description of SED/CSED Model

The derivation of the SED model is described in detail in Rashid et al. 2000, but for continuity we give here a summary of the relevant material. The development is fashioned after the well-known path independent J-integral approach developed by Rice in the sixties (Rice 1968) for the analysis of strain concentration by notches and cracks, which revolutionized the field of Fracture Mechanics. It will be shown that an exact equivalence exists between the SED/CSED model and Rice's J/J_C formulation.

Consider a homogeneous body subjected to a two-dimensional deformation field, containing a defect or a crack that can be represented by a notch of the type shown in Figure 2-8.

Define the strain energy density $\overline{U}$:

$$\overline{U} = \int \sigma_{ij}\, d\varepsilon_{ij} \tag{2-1}$$

where σ_{ij} and ε_{ij} are the stresses and the strains respectively. The J-integral is defined by

$$J = \oint_{\Gamma} \overline{U} dy - \oint_{\Gamma} F \cdot \frac{\partial u}{\partial x}\, ds \tag{2-2}$$

In eq. 2-2, the integration is performed over the curve surrounding the notch tip. F is the traction vector such that it is positive in the direction of the outward normal along Γ, i.e. $f_i = \sigma_{ij} n_j$, u is the displacement vector, and ds is an element of arc length along Γ. The integral in eq. 2-2 is path independent; i.e., the value of J does not change if another contour enclosing the notch is chosen; proof of path dependence of the J-integral is given by Rice in his classic paper [Rice 1968].

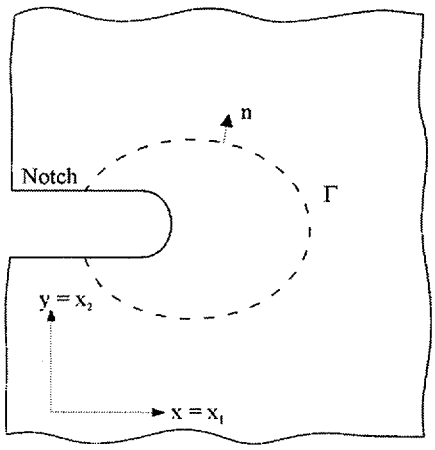

Figure 2-8
Flat Surface Notch in Two-Dimensional Deformation Field

The model development will now focus on a fuel rod geometry and material condition. During service, damage accumulation by two sources, fast-neutron fluence and hydrogen absorption affects the ability of the cladding to withstand mechanical loading by PCMI or pressure forces. The effects of irradiation damage is to homogenize the material, including reducing anisotropy, to increase the yield and ultimate strengths and to decrease the uniform and total elongation values. The damage caused by hydrogen, on the other hand, is heterogeneous and is of two types. The first type consists of circumferentially oriented hydride platelets distributed in the cladding in a radially varying concentration gradient. In some cases, the hydrides are driven towards the cladding outer region, under the effects of temperature and stress gradients, forming a narrow (<50μm) hydride-rich outer rim beneath the corrosion layer [Fuketa et al. 1996]. The hydrogen concentration in the hydride rim can exceed 2000 ppm, with the average hydrogen

concentration decreasing to one or two hundred ppm closer to the inner surface. The second type of damage is the formation of hydride lenses as a result of oxide spallation [Papin et al. 1996]. These hydride lenses are localized discontinuities, which under worst case conditions can penetrate to almost mid wall. They have the effect of a notch, causing strain concentration in the surrounding Zircaloy material. Such hydride concentration can be characterized as a notch-type discontinuity, which lends itself quite naturally to the application of the J-integral methodology. Other, but less severe, forms of discontinuities, which can be treated in the same way, are surface hydrides and small incipient cracks. Under high burnup, given the right loading condition, there is ample opportunity for cladding failure to initiate from one such discontinuity. Since the exact location and geometry of the offending discontinuity is not known a priori, other than that it exists somewhere in the cladding cross section, the adoption of a fracture-toughness based failure criterion would not be useful. Thus, the purpose is to formulate a failure model based on notch-type simulation of a discontinuity, but without having to prescribe the exact geometry or location of the notch.

To this end consider Figure 2-9, which is a cross-section of a fuel rod with a notch-type cladding defect. Owing to the path independence of the J-integral, we are free to take the contour shown by the dashed line, which encloses the entire cross section, consequently enclosing all possible discontinuities. The choice of a discrete notch-type form of damage is mainly to facilitate the mathematical derivations, but the exact form of the damage is not important. We wish to estimate the value of J without analyzing the cracked body. Now, for the contour line chosen, we have,

$$F = 0 \text{ at } r = r_o$$

$$F \approx 0 \text{ at } r = r_i$$

$$F^+ = F^- \text{ at } \theta = 0$$

Under internal pressure, the line integral of the traction term,

$$\oint_{\Gamma} F \cdot \frac{\partial u}{\partial x}\, ds = 0 \text{ at the closed ID surface.}$$

The traction term in eq. 2-2 drops out, and J becomes, using Green's theorem,

$$J = \oint_{\Gamma} \overline{U} dy = \int_{A} \frac{\partial U}{\partial x}\, dx dy \qquad (2\text{-}3)$$

From eq. 2-3 it can be noted that, at the time of failure initiation, J becomes J_C (the fracture toughness), and correspondingly $\overline{U}$ becomes $\overline{U}_c$, which we designate as the critical strain energy density (CSED). Using the definition in eq.1, this can be written as,

$$\overline{U}_c = \int_{0}^{\varepsilon_f} \sigma_{ij}\, d\varepsilon_{ij} \qquad (2\text{-}4)$$

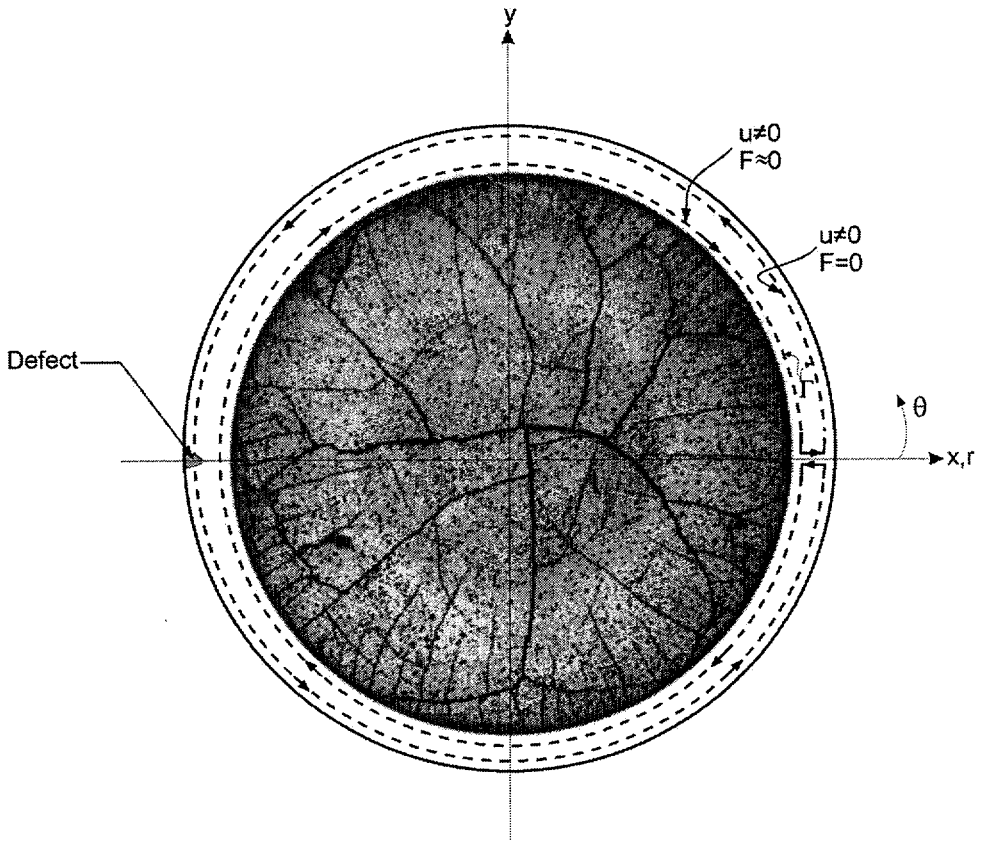

Figure 2-9
Cross-Section of Fuel Rod with Contour Line Surrounding Defect Tip

where ε_f is the material failure strain, which is the total elongation in a uniaxial test; in multi-dimensional tests, ε_f becomes a function of the biaxial or triaxial stress ratios. Having thusly established equivalence between CSED and J_C, we can henceforth concentrate on the development of the CSED as a failure model for cladding material. Equation 2-4 states that the CSED is quantified from stress-strain data obtained from material property tests. The functional dependence of CSED on damage mechanisms, such as hydride lenses, hydride rim, spalled oxide, ID or OD cracks, etc., is reflected in the material property data for irradiated cladding with representative corrosion and hydride conditions to those encountered in high burnup fuel rods.

2.3.2.2 Development of CSED for Irradiated Zircaloy Cladding

The critical strain energy density (CSED) is developed from material property tests as a function of material conditions, including temperature, fast fluence, outer surface corrosion, hydrogen concentration, and hydride morphology. The database of mechanical property tests on irradiated cladding material used to develop the CSED relations contains a variety of cladding designs, irradiation conditions, oxide thickness levels, and testing conditions (temperature and strain rate). These tests were conducted as part of fuel performance monitoring programs sponsored by EPRI and the U.S. Department of Energy (DOE) to evaluate intermediate and high burnup fuel

behavior [Newman 1986; Smith et al. 1994a; Smith et al. 1994b]. A summary of the important characteristics of the database is shown in Table 2-5. The test samples were obtained from fuel rods that had achieved fuel rod average burnup levels between 25 GWd/tU and 62 GWd/tU. A few samples extracted from high burnup rods exhibited oxide spallation and localized hydrides. Like the ultimate tensile strength and total elongation data from which it is derived, the CSED data obtained from mechanical property tests on irradiated cladding implicitly includes all the mechanical property degradation mechanisms caused by irradiation, such as fast neutron damage, zirconium hydride content and orientation, and localized hydride accumulations.

The CSED ($\overline{U}_c$) is obtained by calculating the contribution from each deformation regime (elastic and plastic) separately and adding them together to obtain the total CSED. The material parameters used in the calculation of the CSED are depicted in Figure 2-10, which shows a schematic of the stress-strain curve for Zircaloy.

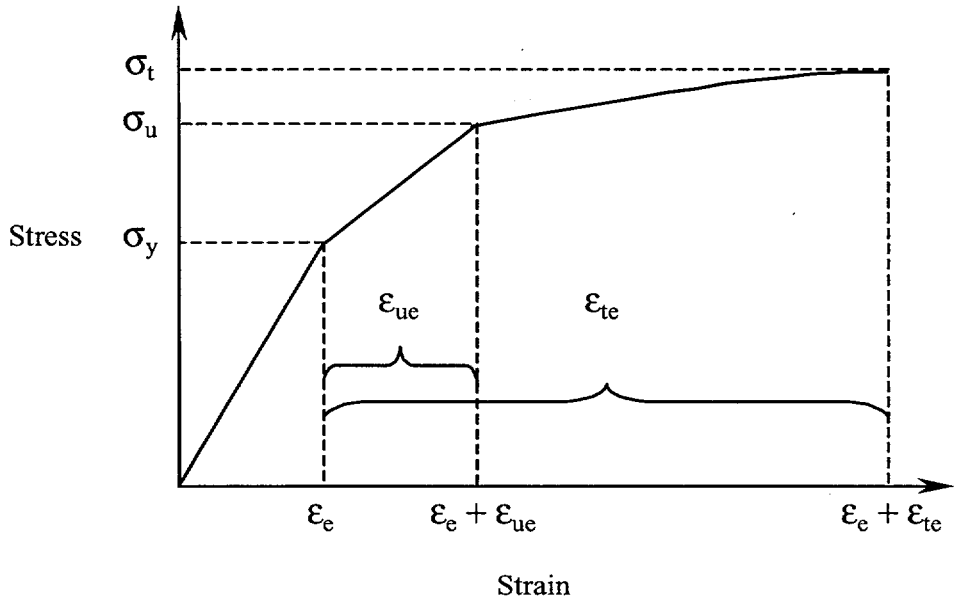

Figure 2-10
Schematic of the Stress-Strain Curve Illustrating CSED Calculations

The elastic strain energy component ($\varepsilon \leq \varepsilon_e$) is derived from Hooke's Law and is given by;

$$\overline{U}_e = \frac{s_y^2}{2E} \tag{2-5}$$

where σ_y is the yield stress and E is Young's Modulus.

The calculation of the CSED in the plastic regime is based on the assumption that the material true stress-true strain curve can be represented by the following relationship from MATPRO [Hagrman1995]:

$$\sigma = K\varepsilon^n \left(\frac{\dot{\varepsilon}}{\dot{\varepsilon}_o}\right)^m \quad \text{for} \quad \varepsilon_e < \varepsilon < \varepsilon_e + \varepsilon_{te} \tag{2-6}$$

where σ is the true stress; ε is the true strain; $\dot{\varepsilon}$ is the strain rate; and K, n, and m are material constants obtained from MATPRO.

The total strain energy in the plastic regime ($\varepsilon > \varepsilon_e$) can be obtained by integrating eq. 2-6 between the elastic limit (ε_e) and the total elongation as shown in eq.2- 7.

$$\overline{U}_p = \int_{\varepsilon_e}^{\varepsilon_e + \varepsilon_{te}} K\varepsilon^n \left(\frac{\dot{\varepsilon}}{\dot{\varepsilon}_o}\right)^m d\varepsilon \tag{2-7}$$

This expression can be simplified by evaluating eq.2-6 at the elastic limit, which yields,

$$K\left(\frac{\dot{\varepsilon}}{\dot{\varepsilon}_o}\right)^m = \sigma_y^{1-n} E^n \tag{2-8}$$

Substituting eq. 2-8 into eq. 2-7, integrating and evaluating the result at the integration limits gives the plastic strain energy component as:

$$\overline{U}_p = \frac{\sigma_y^{1-n} E^n}{n+1} \left[(\varepsilon_e + \varepsilon_{te})^{n+1} - \varepsilon_e^{n+1} \right] \tag{2-9}$$

The total CSED is simply the sum of the elastic and plastic strain energy components, i.e.,

$$\overline{U}_c = \overline{U}_e + \overline{U}_p \tag{2-10}$$

2.3.2.3 Data Adjustment Factors

There are three important effects that must be considered before using the data from mechanical property tests to establish a CSED relation for irradiated Zircaloy cladding. These are material anisotropy, multiaxial stress-state, and strain rate effects.

Anisotropy: Irradiated Zircaloy exhibits significant reduction in anisotropy because of irradiation damage. Existing mechanical property data, obtained for temperatures below the level required to anneal irradiation damage, demonstrate that irradiated Zircaloy cladding exhibits isotropic or near-isotropic behavior [Murty and Mahmood 1991]. The effect of cladding anisotropy need be considered only when combining irradiated and unirradiated data.

Multiaxial Stress-State: PCMI-induced stresses are generally biaxial, a condition that needs to be accounted for in the CSED Model. Therefore, the total elongation values obtained from the uniaxial ring tension and axial tube tension tests were adjusted to account for biaxiality effects

on ductility. The total elongation values from the uniaxial tests were reduced using an adjustment factor developed based on material test data obtained by Koss and Andersson that show that effects of hydrogen content and stress ratio on total elongation [Fan and Koss 1985; Andersson and Wilson 1978].

The biaxiality adjustment factor used for the ring and axial tension data was developed from mechanical property tests reported by Koss on Zircaloy sheet material under different loading and hydrogen conditions. Figure 2-11 was used to develop a relationship between a strain reduction factor and hydrogen. It was assumed in the developing the adjustment factor that PCMI conditions are represented by a plane strain condition in the axial direction, i.e. $\varepsilon_z = 0$. The following relationship was developed from a numerical fit of the $\varepsilon_{2f} = 0$ data reported by Koss;

$$f_b = 0.33 \cdot e^{-.1.19x10^{-3} \cdot H_c} \qquad (2\text{-}11)$$

where:

f_b is the biaxiality adjustment factor

H_c the average hydrogen content for the sample (ppm)

The adjusted total plastic strain for biaxial conditions is calculated using the following expression:

$$\varepsilon_c = \varepsilon_{uni} \cdot f_b$$

where

ε_c is the adjusted total plastic strain for biaxial conditions

ε_{uni} is the uniaxial total plastic strain measured in tube or ring tension tests

The adjusted strain values are used in the calculation for the CSED values and total elongation values, and are applied to transient PCMI conditions.

Strain Rate Effects: The rapid PCMI loading caused by RIA transients suggests that strain rate effects should be considered in the CSED development. High strain rates can reduce the ductility; however, the limited experimental data on irradiated Zircaloy above 288°C show little effect of strain rate in the range observed in RIA tests. It should be mentioned, however, that the SED values calculated in FALCON using the MATPRO true-stress-true-strain equations are strain-rate dependent. This means that for the RIA events, where the strain rates are somewhat higher than the material property data used in the CSED correlation, FALCON calculates slightly higher SED values. Thus FALCON's predictions of RIA response would be conservative with respect to the CSED correlation.

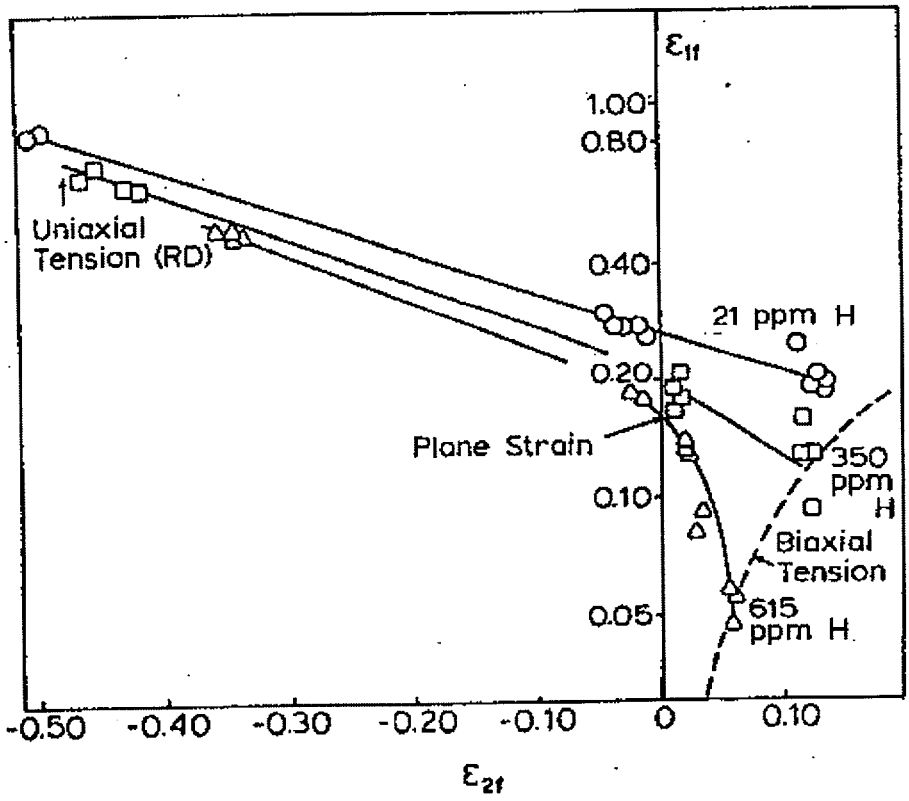

Figure 2-11
Zircaloy Sheet Ductility Data for Various Loading Conditions [Koss, et. al.]

2.3.2.4 CSED Correlation

The CSED correlation used as part of the cladding model for RIA events was determined from the results of the mechanical property tests as a function of temperature, fast fluence, and the hydrogen concentration, or alternatively the oxide thickness. For high burnup Zircaloy cladding, hydride content and distribution can have an important impact on the mechanical response. Hydrogen pickup from outer surface corrosion is the primary source of hydrogen in Zircaloy cladding. Consequently, the hydride content is generally proportional to the oxide layer thickness. In developing a CSED correlation for high burnup Zircaloy, the ratio of the sample oxide thickness to cladding thickness (R_{ox}) was used as the correlation parameter. By using this parameter to correlate the CSED results, it is possible to compare results for different initial cladding types, e.g. 14x14 vs. 17x17.

The CSED values from the mechanical property tests listed in Table 2-5 are shown in Figure 2-12 for temperatures above 280°C and in Figure 2-13 for temperatures below 150°C. The legend shown in Figure 2-12 designates which CSED values correspond with the axial tension tests, the uniaxial ring tension tests and the burst tests. A review of the data indicates that the CSED data

from the ring tension tests are generally larger than the burst and axial tension CSED data. The higher CSED values for the ring tension tests may be related to bending within the gauge section during the test, which will increase the measured total elongation for these specimens. Bending artifacts would be most notable in ductile samples. On the other hand, the CSED obtained from axial tension data generally reside below the ring and burst data. The CSED data from burst tests reside between the CSED values from ring and axial tension tests. All the different data sets display a decreasing trend as a function of R_{ox}. The data from samples with non-spalled oxide layers shown in Figure 2-12 does not show significant temperature dependence in the 280°C to 400°C range. However, only a limited number of tests were performed at the high temperature and insufficient data is available to fully quantify the effect of temperature on the CSED in the temperature range from 280°C to 400°C.

The CSED data obtained from mechanical property tests on samples with spalled oxide layers are indicated by the solid symbols. These data reside at R_{ox} values above 0.10 and the CSED values are generally below 10 MJ/m^3. As seen in Figure 2-11, the CSED data from samples with spalled oxide layers display a natural separation from the data with non-spalled oxide layers.

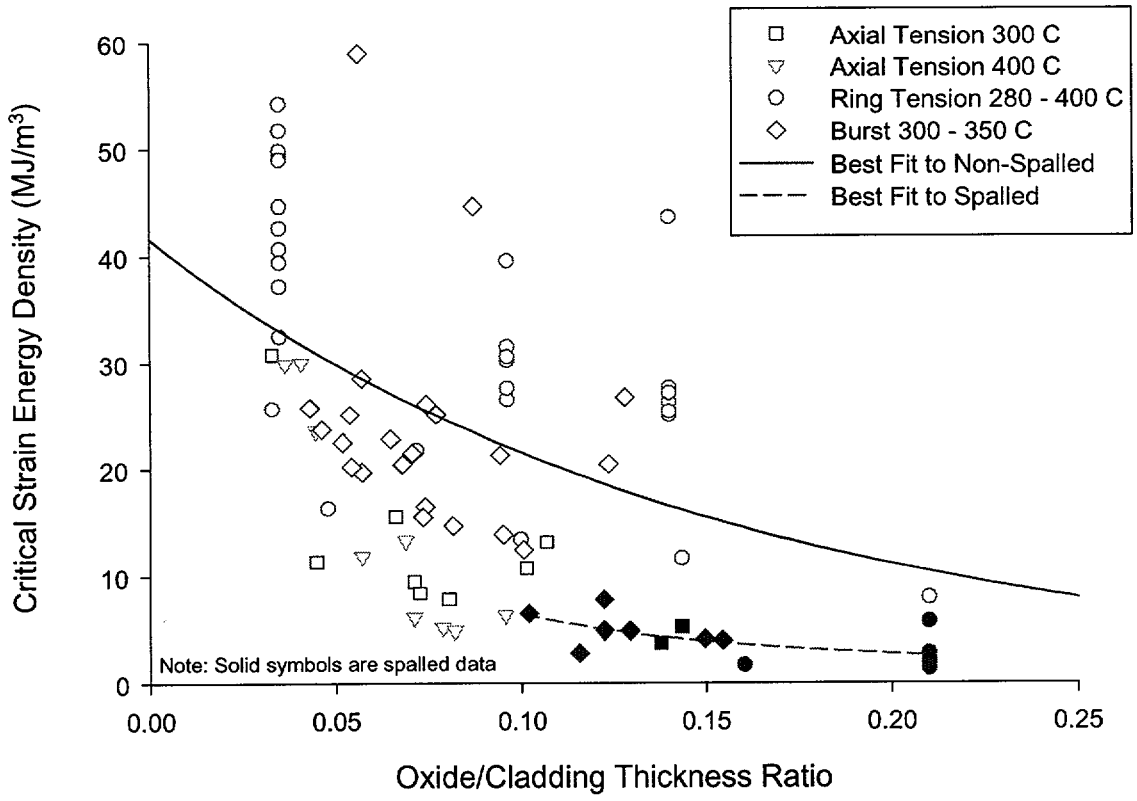

Figure 2-12
CSED data as a function of oxide-to-cladding thickness ratio developed from mechanical property tests at temperatures above 280°C on cladding irradiated to burnup levels between 50 and 65 GWd/tU. The data from samples with outer surface oxide spallation are indicated by the solid symbols. The best-fit correlations are shown for comparison.

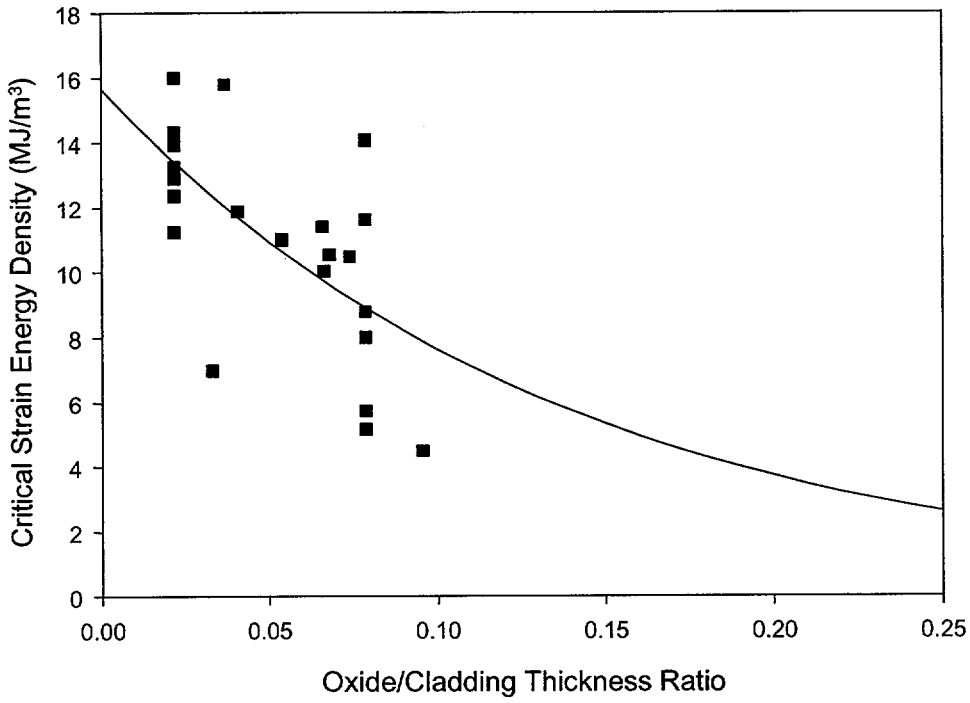

Figure 2-13
CSED data as a function of oxide-to-cladding thickness ratio developed from mechanical property tests at temperatures below 150°C on cladding irradiated to burnup levels between 50 and 65 GWd/tU. None of these data points were from cladding with spalled oxide layers. The best-fit correlations are shown for comparison.

A numerical fit to the data was conducted to develop a correlation between the CSED and oxide to thickness ratio (R_{ox}). To facilitate the fitting process, the data above 280°C were divided into two data sets that represent different material conditions: one for samples without oxide spallation and one for samples with oxide spallation. Best-fit curves were developed for each data set (non-spalled and spalled) by fitting to all the CSED data (ring, axial, burst) in each data set. For the CSED data from samples with non-spalled oxide layers, an exponential expression was used to obtain the functional form of CSED correlation. An exponential functional dependence was selected to allow for saturation of the CSED to a low, non-zero value when extrapolated to high R_{ox} values. Because the data from samples with spalled oxide thickness layers displays less of a dependence on R_{ox}, a power law was used to develop the CSED correlation.

The resulting numerical fits for the CSED of non-spalled and spalled cladding at temperatures above 280°C are:

For non-spalled cladding,

$$\overline{U}_c = 41.5 \cdot e^{-6.6 \cdot R_{ox}} \text{ with } 0.03 < R_{ox} < 0.23 \qquad (2\text{-}12)$$

For spalled cladding,

$$\overline{U}_c = 0.371 \cdot R_{ox}^{-1.24} \text{ with } 0.1 < R_{ox} < 0.23 \quad (2\text{-}13)$$

where

$\overline{U}_c$ is the critical strain energy density (MJ/m^3)

R_{ox} is the ratio of the outer surface zirconium oxide layer thickness to cladding thickness (unitless)

For non-spalled cladding loaded below 150°C, the CSED correlation is given by;

$$U_c = 15.67 \cdot e^{-7.19 \cdot R_{ox}} \quad (2\text{-}14)$$

Equations 2-12 through 2-14 represent best-fit correlations to all CSED values in each data set and the CSED data is scattered about these curves. As can be seen in Figures 2-12 and 2-13, the scatter in the data is large and is attributable to the variability in the material condition for irradiated cladding, test conditions such as temperature and loading direction, and sample artifacts such as bending within the gauge section. Unfortunately for irradiated material, this level of scatter is inherent to the data and improvements in future tests are needed to eliminate some of these sources of scatter. An attempt has been made to address data scatter caused by outer surface oxide spallation by separating the data into spalled and non-spalled specimens. As seen in Figure 2-12, the data show a natural separation in the CSED values between the data from non-spalled specimens and spalled specimens.

As a means to evaluate the influence of the data scatter within the non-spalled CSED data set on the best-fit correlation, two additional numerical fits were performed: a best-fit to the non-spalled CSED data from the tube burst tests and a lower bound fit to the non-spalled CSED data from the tube burst and ring tension tests. Tube burst tests and ring tension tests yield hoop direction mechanical properties. Since PCMI loading is primarily oriented in the hoop direction, it can be argued that ring and tube burst mechanical tests are more applicable to PCMI loading conditions. Furthermore, the burst test CSED data displays the least amount of data scatter and also represents the mechanical properties in the hoop direction under biaxial stress conditions. Unfortunately, the amount of data available for tube burst tests is limited making it more difficult to use this data to develop a versatile CSED model that can be applied to transient fuel rod analysis and data interpretation.

A comparison of the correlation in Equation 2-12 and the two alternative fits is shown in Figure 2-14. The lower bound fit to the non-spalled tube burst and ring tension CSED data is well below the best-fit Equation 2-12 or the best fit of the tube burst data. This correlation accounts for the lower bound scatter of the data and represents a conservative measure of cladding failure.

As seen in Figure 2-14, the best fit to the non-spalled tube burst data deviates only slightly from the best-fit to all the non-spalled data (Equation 2-12). The largest difference occurs at low

oxide thickness layers ($R_{ox} < 0.1$). For these conditions, the ductility exhibited by the ring tension tests is larger than that for the tube burst tests, even after the biaxiality correction factor is applied to the ring tension data. This could be caused by the influence of sample bending in the ring tension tests. However, at R_{ox} values greater than 0.1, very little difference exists between the two correlations. Such comparison supports the approach used to develop the correlation given by Equation 2-12.

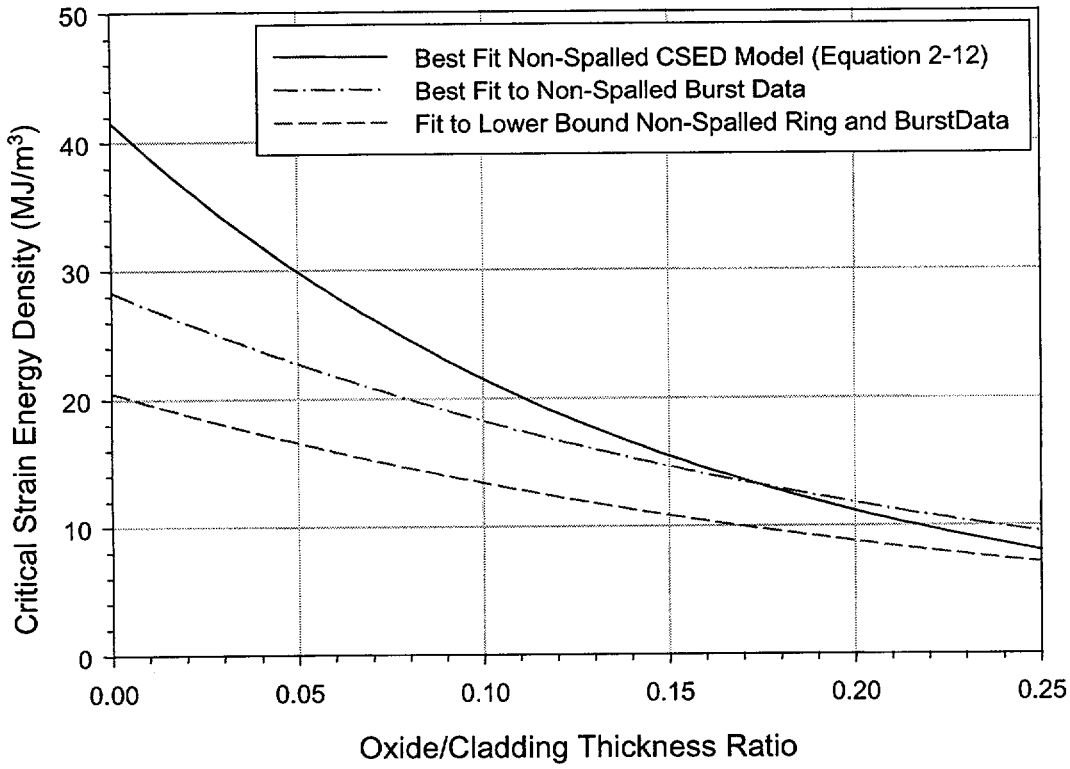

Figure 2-14
Comparison of the Best-Fit CSED model (T > 280°C) developed using all the data from tests on non-spalled oxide samples (Equation 2-12) with two alternative fits developed using the data from the tube burst and ring tension tests on non-spalled oxide cladding samples.

2.3.2.5 Total and Uniform Elongation Models

To compare the SED/CSED approach with other strain-based criteria, cladding integrity models based on the total elongation (TE) and uniform elongation (UE) strains have been developed from the same material property data used for the CSED correlation. In the case of the TE strain, the biaxiality adjustment factor shown in Equation 2-11 was applied to the data from uniaxial ring and axial tension tests. The elastic strain obtained from the elastic modulus and the yield stress was added to the total and uniform plastic strain values measured in the mechanical property tests. The TE strain data is shown in Figure 2-15 and the UE data is shown in Figure 2-16 as a function of the oxide-to-thickness ratio. The data from samples with spalled oxide layers

has been separated from the non-spalled data for clarification. Also shown for comparison are the correlations from the data fit exercise. As can be seen, the trend with oxide thickness is similar to the CSED correlation. The data scatter is equal to or greater than that for the CSED data shown in Figures 2-12 and 2-13. The ability of these models to separate failures from non-failed RIA-simulation tests is discussed in Section 2.4.3.

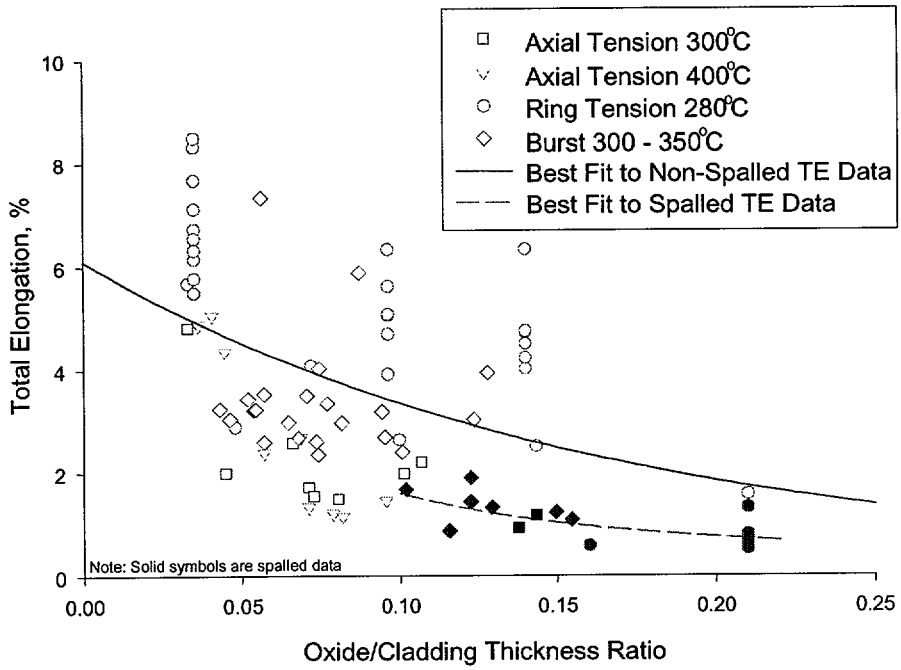

Figure 2-15
Total elongation (TE) data as a function of oxide-to-cladding thickness ratio developed from mechanical property tests on irradiated cladding at temperatures above 280°C. The data from samples with outer surface oxide spallation are indicated by the solid symbols. The best-fit correlations are shown for comparison.

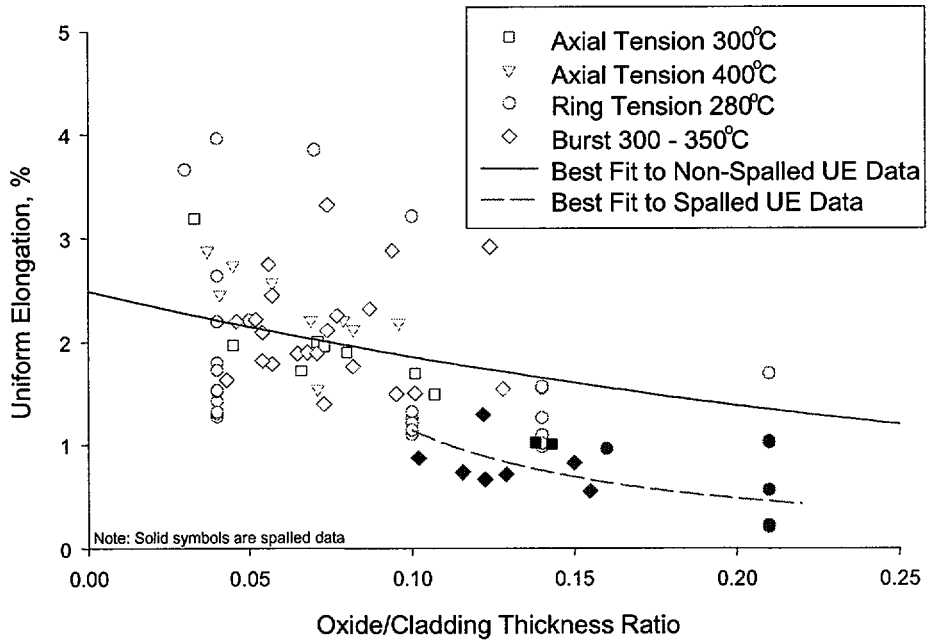

Figure 2-16
Uniform elongation (UE) data as a function of oxide-to-cladding thickness ratio developed from mechanical property tests on irradiated cladding at temperatures above 280°C. The data from samples with outer surface oxide spallation are indicated by the solid symbols. The best-fit correlations are shown for comparison.

2.3.2.6 Summary

A cladding failure model applicable to PCMI conditions under operational and accident transients has been developed for irradiated Zircaloy cladding based on the strain energy density (SED) concept. The SED/CSED model is derived from the J-integral methodology used in fracture mechanics evaluations, by establishing exact equivalence between SED and J, and CSED and J_C. It allows for the treatment of damaged material without explicitly modeling local defects or performing fracture mechanics analysis. A critical strain energy density (CSED), which defines the material limit for mechanical loading, was developed as a function of temperature and outer surface oxide layer thickness from mechanical property tests conducted on irradiated Zircaloy cladding. An important aspect of this approach is the fact that the mechanical property data used to derive the CSED includes material that contains incipient hydride and irradiation damage similar to that present in irradiated cladding.

2.4 Analysis of RIA-Simulation Experiments

Detailed fuel behavior analyses were performed for key RIA-simulation experiments using the EPRI fuel behavior code FALCON [Montgomery and Rashid 1996; Yang et al. 2000]. The objectives of these analyses can be separated into three different goals. First, these analyses were used to assist in the interpretation of the experimental results by providing insights into the

thermal and mechanical performance of the fuel and cladding. From the results of these analyses, it was possible to assess the evolution of cladding stresses and temperatures to determine the cladding state at the time of peak stress. Second, it was possible to demonstrate that the mechanisms important for understanding fuel behavior have been identified through comparison of the calculated results with the experimental observations and post-test examination results. The FALCON analyses of RIA experiments assisted in separating the effects of cladding ductility and fission gas swelling on the fuel behavior exhibited in the experiments. Third, these analyses were used to validate the analysis capabilities of FALCON.

2.4.1 FALCON Description

FALCON is a two-dimensional transient fuel behavior program developed to analyze the response of LWR fuel rods during RIA, LOCA and other transient conditions [Montgomery et al. 1997b]. FALCON, which is an improved version of FREY [Rashid et al. 1994], utilizes a coupled thermal and mechanical finite element methodology to represent the transient behavior of the fuel column, cladding, and gap. A complete fuel pellet mechanical constitutive model is used that includes pellet cracking, creep, plasticity, and thermal expansion. The effects of burnup and fast neutron fluence are included in the thermal and mechanical properties of the fuel and cladding, as well as, on the radial power distribution. Recently, modifications have been incorporated into FALCON to calculate the sodium coolant temperature heatup during the CABRI experiments. Earlier analyses used estimated heat transfer coefficients and coolant temperatures to model the fuel-sodium heat transfer.

At this time, FALCON does not include a gaseous swelling model in the high burnup rim region for rapid transients such as an RIA. It has been postulated by some that an additional rapid pellet expansion process exists that is driven by the large inventory of fission gas resident in the pellet periphery [Lemoine, 1997, Papin, 1996]. However, evidence supporting the potential for rapid gas bubble expansion in the rim region has not been found in post-test examinations of high burnup test rods such REP Na-4 and REP Na-5 [Lespiaux et al 1997]. Furthermore, validation of FALCON using RIA test results from UO_2 fuel rods demonstrates that pellet thermal expansion is the primary driving force for PCMI during rapid power deposition [Montgomery 1996a].

2.4.2 FALCON Validation for RIA Analysis

The RIA-simulation tests analyzed with FALCON are summarized in Table 2-6. The tests selected for the FALCON validation include tests conducted in the CABRI sodium loop at an initial temperature of 290°C and the NSRR test capsule with 25°C stagnant water. Tests with both narrow and wide pulses were selected to evaluate the influence of pulse width on the test rod response. Sodium temperature thermocouple measurements, in-pile cladding axial elongation and residual cladding hoop strains have been used to validate the FALCON capabilities for RIA analyses.

Table 2-7
RIA-Simulation Tests used in the FALCON Validation

Test	Peak Pellet Burnup (GWd/tU)	Oxide Layer (microns)	Fuel Type	Pulse Width (msec)	Maximum Radial Average Fuel Enthalpy (cal/gm)	Fuel Enthalpy at Failure (cal/gm)
CABRI REP Tests in 280°C Sodium at 0.5 MPa						
Na-1	65	>80 – spall	17x17	9.5	115	30
Na-2	33	10	17x17	9.5	220	
Na-3	52	50	17x17	9.5	138	
Na-4	62	85	17x17	70	81	
Na-5	64	20	17x17	9.1	113	
Na-8	60	120 - spall	17x17	78	105	83
Na-10	64	>80 - spall	17x17	31	112	79
NSRR PWR and BWR Tests in 25°C Water at 0.1 MPa						
HBO-1	50	40-50	17x17	4.4	73	60
HBO-2	50	30-40	17x17	6.9	37	
HBO-3	50	22	17x17	4.4	74	
HBO-4	50	18	17x17	5.4	50	
HBO-5	44	35-60	17x17	4.4	80	77
HBO-6	49	20-30	17x17	4.4	88	
TK-1	38	7	17x17	4.4	125	
TK-2	48	15-35	17x17	4.4	107	60
TK-4	50	20	17x17	4.4	98	
FK-1	45	20-40	8x8BJ	4.4	130	
FK-2	45	20-40	8x8BJ	5.3	70	
FK-4	56	~20	8x8	4.4	140	
FK-5	56	~20	8x8	7.3	70	
FK-6	61	~25	8x8	4.3	131	70
FK-7	61	~25	8x8	4.3	129	62
FK-8	61	~25	8x8	7.3	65	
FK-9	61	~25	8x8	5.7	90	86

A comparison of the CABRI REP Na-4 thermocouple response within the sodium coolant at 48 cm (near the top of the fuel stack) and the calculated sodium temperature at different locations in the FALCON model is shown in Figure 2-17. The peak sodium temperature measured by the two thermocouples located 120° azimuthally apart varied from 373°C to 396°C. The calculated sodium temperatures at 46 cm reached a peak of 383° C and the calculated sodium temperatures at 52 cm reached a peak at 388° C. The calculated results are within the scatter of the in-pile measurements.

The cladding axial elongation response measured using an in-pile LVDT device is shown in Figure 2-18 for CABRI REP Na-4. Also shown for comparison is the calculated cladding elongation. FALCON calculates a slightly lower peak cladding elongation (3.7 mm versus 4.2 mm), however, the calculated cladding elongation response is consistent with the overall trend in the cladding elongation measurements after the power pulse. The difference between the measured and calculated peak cladding elongation is 13% and is related to differences in the power pulse and axial power distribution used in the analysis and the actual experimental conditions.

A comparison of the calculated and measured permanent cladding radial displacements for REP Na-5 is shown in Figure 2-19 as a function of axial position. Two different azimuthal traces are shown to indicate the variation in the measured data. The calculated results reside in the mid-range of the experimental measurements in the peak power location. FALCON has a tendency to calculate slightly higher cladding radial displacements at the ends of the test specimen. This could be due to uncertainty in the axial power shape used in the analysis.

Figures 2-20 and 2-21 show a comparison between the measured and predicted residual cladding hoop strains (Figure 2-20) for the CABRI REP Na tests and the measured and predicted cladding and fuel axial elongation for the CABRI and NSRR tests analyzed with FALCON (Figure 2-21). The calculated and measured cladding hoop strain results shown in Figure 2-20 represent the mid-pellet strain at the maximum power location. The error bars shown in Figure 2-20 indicate the variation in the measured data based on the measurement uncertainty. Since most of the datapoints reside near the perfect agreement line (solid line), it can be concluded the FALCON calculates well the cladding radial and axial deformations.

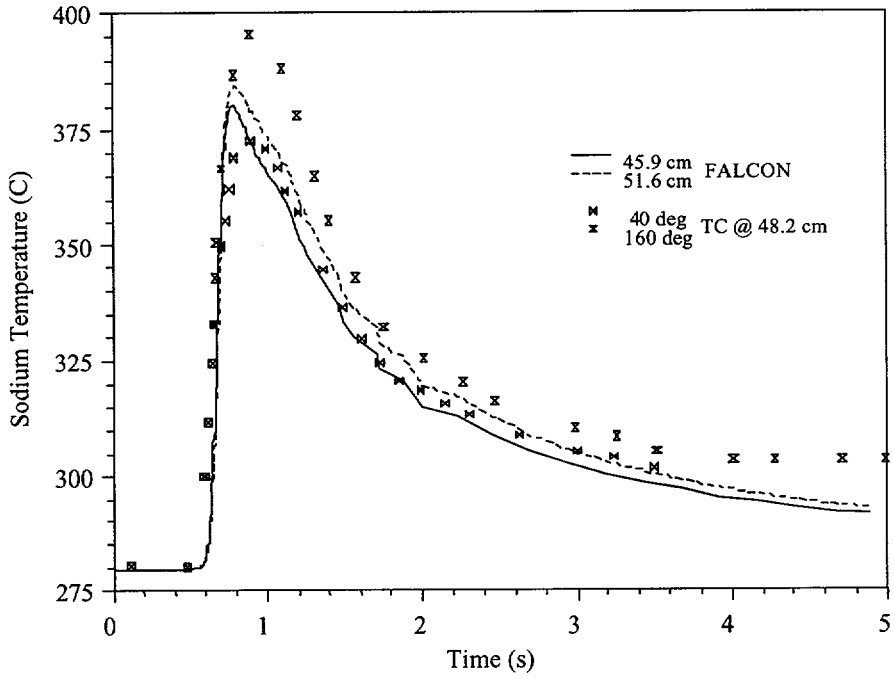

Figure 2-17
Sodium Coolant Temperature during CABRI REP Na-4

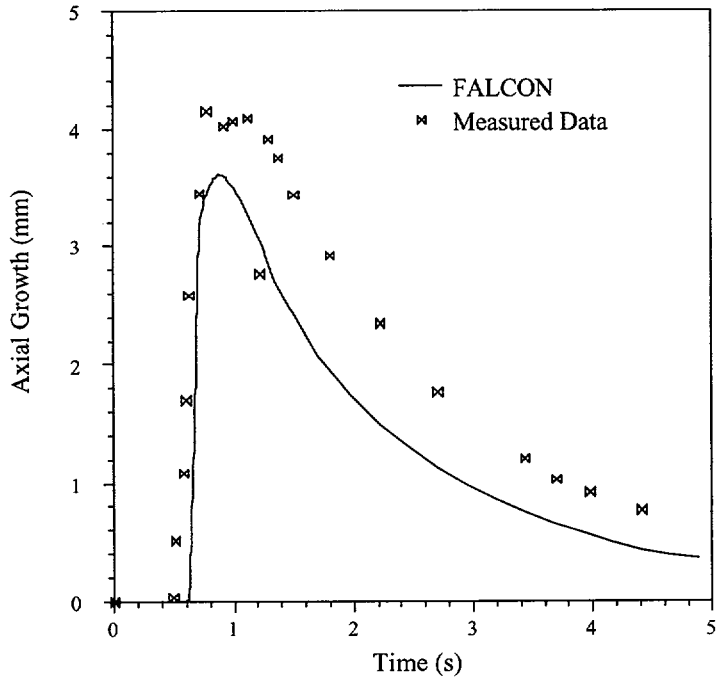

Figure 2-18
FALCON Results and Measured Data for the Time History of the Cladding Axial Elongation in CABRI REP Na-4

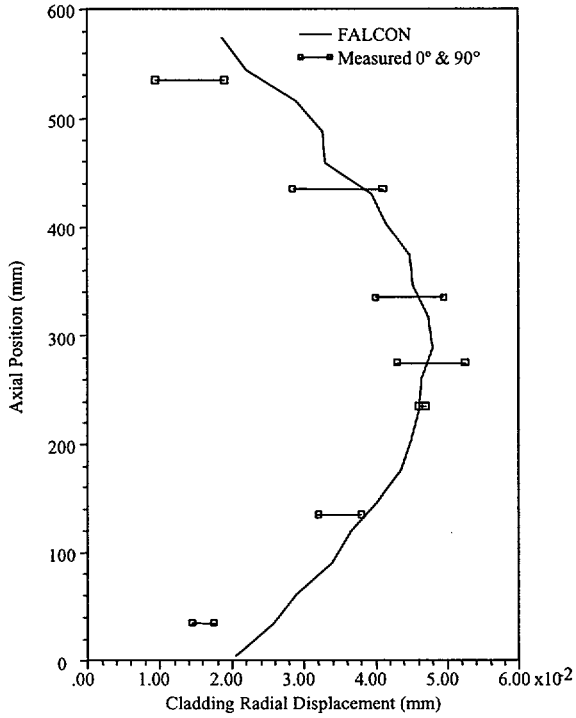

Figure 2-19
Comparison of FALCON and Measured Residual Cladding Radial Displacements for CABRI REP Na-5

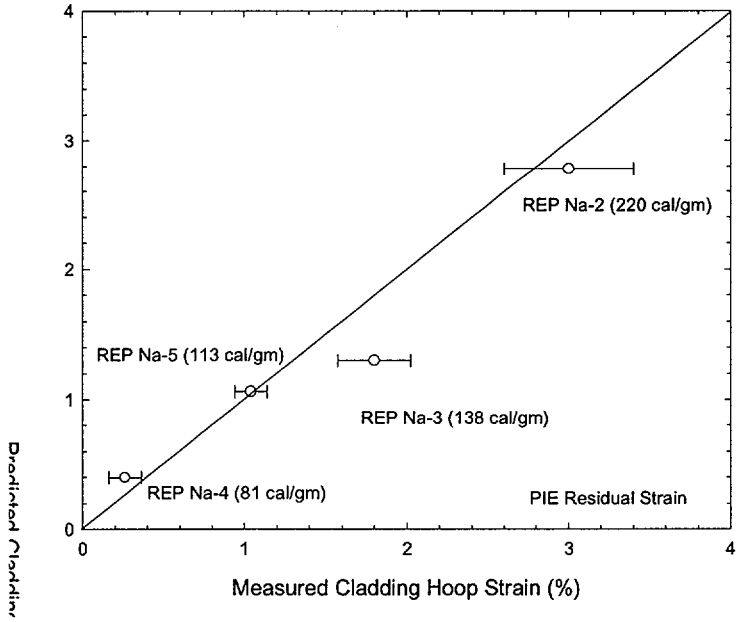

Figure 2-20
Predicted versus Measured Residual Cladding Hoop Strain for Selected CABRI REP Na Tests

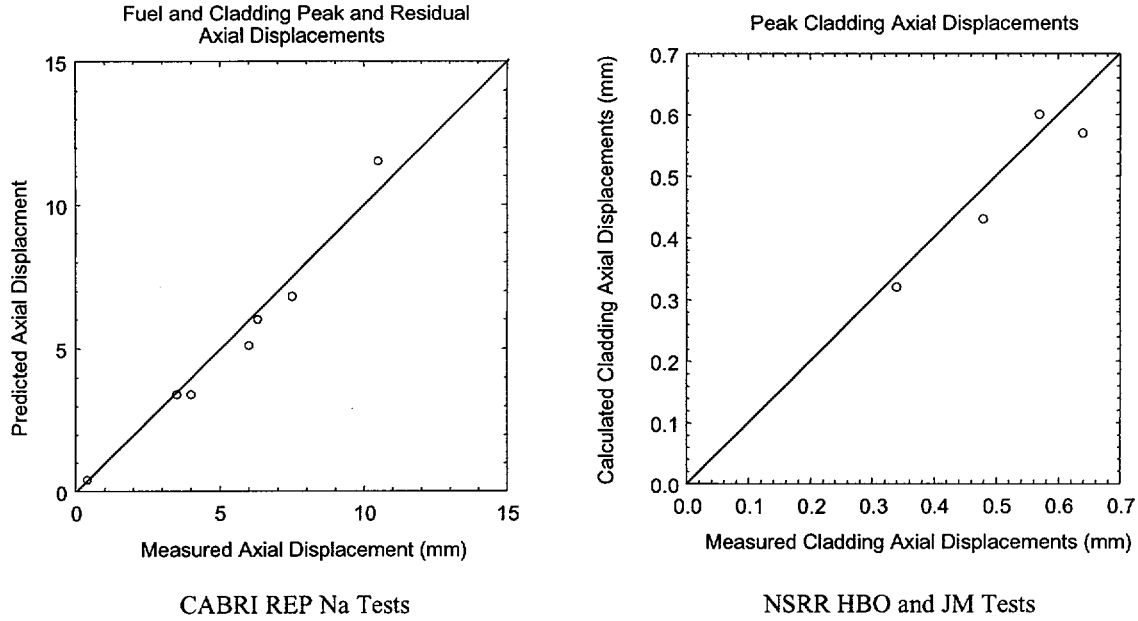

CABRI REP Na Tests

NSRR HBO and JM Tests

Figure 2-21
Predicted versus Measured Peak and Residual Axial Displacements for Selected CABRI REP Na and NSRR tests

2.4.3 Cladding Failure Analysis

The cladding failure evaluation performed within FALCON is based on the CSED/SED approach presented in Section 2.3.2. In this approach, cladding mechanical properties are used to develop the critical strain energy density (CSED) required to initiate material failure from mechanical property tests on irradiated Zircaloy cladding. As summarized in Section 2.3.2.2, the CSED is represented as a function of the material condition, temperature, and loading state. FALCON is then used to calculate the evolution of the strain energy density (SED) within the cladding as a function of cladding stress-state and temperature. An increase in the potential for cladding failure is assumed to occur at the point where the FALCON calculated SED exceeds the CSED for the given cladding condition defined by temperature and oxide thickness.

The SED throughout the cladding is calculated during the PCMI phase for each RIA-simulation test analyzed with FALCON. The SED model in FALCON performs a summation of the product of the stress and strain increment for the three coordinate stresses and strains (radial, axial, and hoop) at every location in the cladding. This quantity is then integrated over the time of the transient to provide the SED (U(t)) as a function of time, ie.;

$$U(t) = \int_0^t \left[\sum \sigma_i \cdot \Delta\varepsilon_i, i = r, \theta, z \right] dt \qquad (2\text{-}14)$$

The maximum calculated SED from Equation 2-14 at the time corresponding to the end of the power pulse or the time of cladding failure determined by in-pile instrumentation is shown in Figure 2-22 for the sodium tests (T > 280°C) and Figure 2-23 for the stagnant water tests (T < 150°C). Also shown for comparison are the appropriate best-fit CSED curves from Figure 2-12 (Equation 2-12) and Figure 2-13 (Equation 2-13) presented in Section 2.3.2. Equation 2-12 represents a best-fit to all the non-spalled CSED data and Equation 2-13 represents a best-fit to all the spalled CSED data. In addition, two alternative non-spalled CSED correlations were developed in Section 2.3 and these correlations are also shown in Figure 2-22 for comparison.

The tests in sodium coolant on rods with non-spalled oxide layers lie below the best-fit CSED curve for non-spalled cladding (Equation 2-12), indicating a low potential for cladding failure. No tests at 300°C using UO_2 rods with non-spalled oxide layers have failed in the CABRI sodium loop. However, the two tests on rods with spalled oxide layers (REP Na-8 and Na-10) reside either on or above the best CSED curve for spalled cladding (Equation 2-12), indicating a high potential for cladding failure. As indicated in the figure (solid symbols), REP Na-8 and REP Na-10 were identified to have experienced cladding failure during the power pulse by in-pile instrumentation and post-test examinations. These results indicate that the presence of significant oxide layer spalling and corresponding localized hydride formation has embrittled the cladding sufficiently to cause cladding failure by PCMI under RIA conditions.

The two alternative CSED fits discussed in Section 2.3 are also shown in Figure 2-22. Both of these curves are only applicable to RIA tests using test rods with non-spalled oxide layers. The lower bound curve does not adequately differentiate between the failed and non-failed rods for the CABRI REP Na tests using UO_2 fuel rods. As shown in Figure 2-23, the lower bound CSED curve predicts that REP Na-2 and REP Na-3 would have failed in the CABRI tests when compared to the calculated SED values for the REP Na experiments. Neither of these rods showed any indication of cladding failure during the experiment or in post-test examinations. Based on these observations, the lower bound CSED correlation does not adequately differentiate between failed and non-failed UO_2 rods tested in the CABRI REP Na program. As a result, this CSED correlation does not represent an alternative to Equation 2-12.

The best-fit of the non-spalled tube burst CSED data resides at the upper boundary of the non-failed CABRI REP Na tests on UO_2 rods. This curve represents an envelope of success based on the CABRI REP Na tests and could serve as an optional lower bound alternative to the Equation 2-12.

Similarly in Figure 2-23, the SED results for the NSRR tests that did not fail reside below the CSED curve for low temperature conditions. It should be noted that the NSRR tests shown in Figure 2-23 are PWR rods because the CSED curve is only applicable to PWR rods tested in NSRR. Tests that experienced failure or contained micro-cracks in the outer region of the cladding reside near or above the CSED curve. Based on these results, the coupled FALCON/SED model displays a reasonable level of success in separating failed and non-failed tests using a CSED limit developed from cladding mechanical property tests on irradiated cladding.

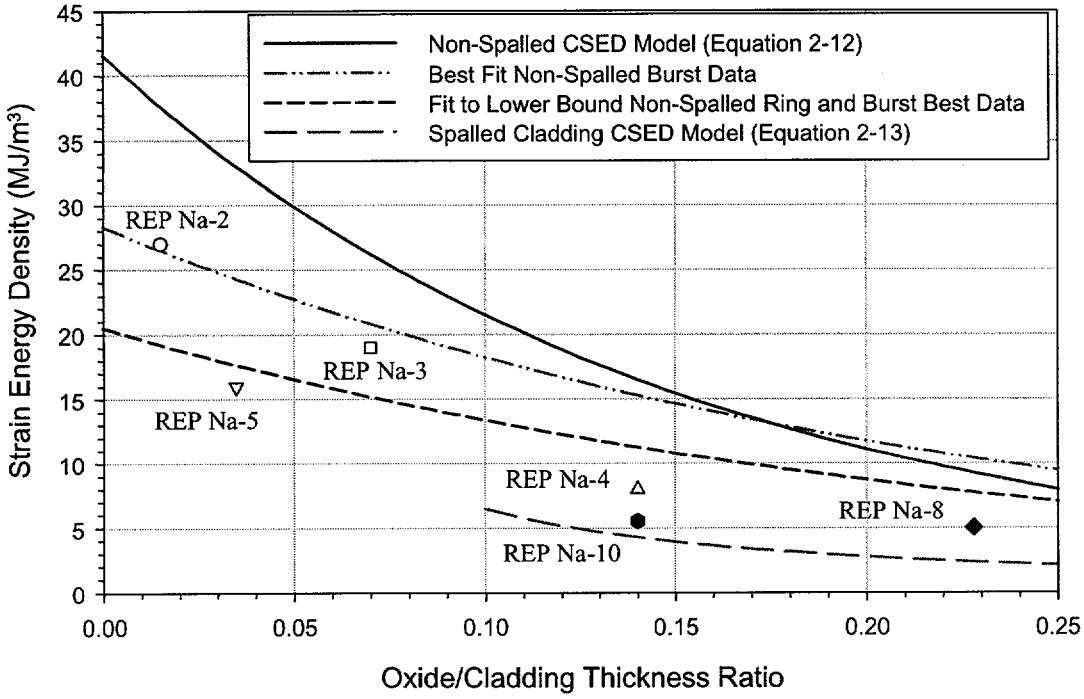

Figure 2-22
Strain energy density results calculated by FALCON for the CABRI REP Na UO_2 test rods. The non-spalled and spalled CSED models for temperatures greater than 280°C are also shown for comparison.

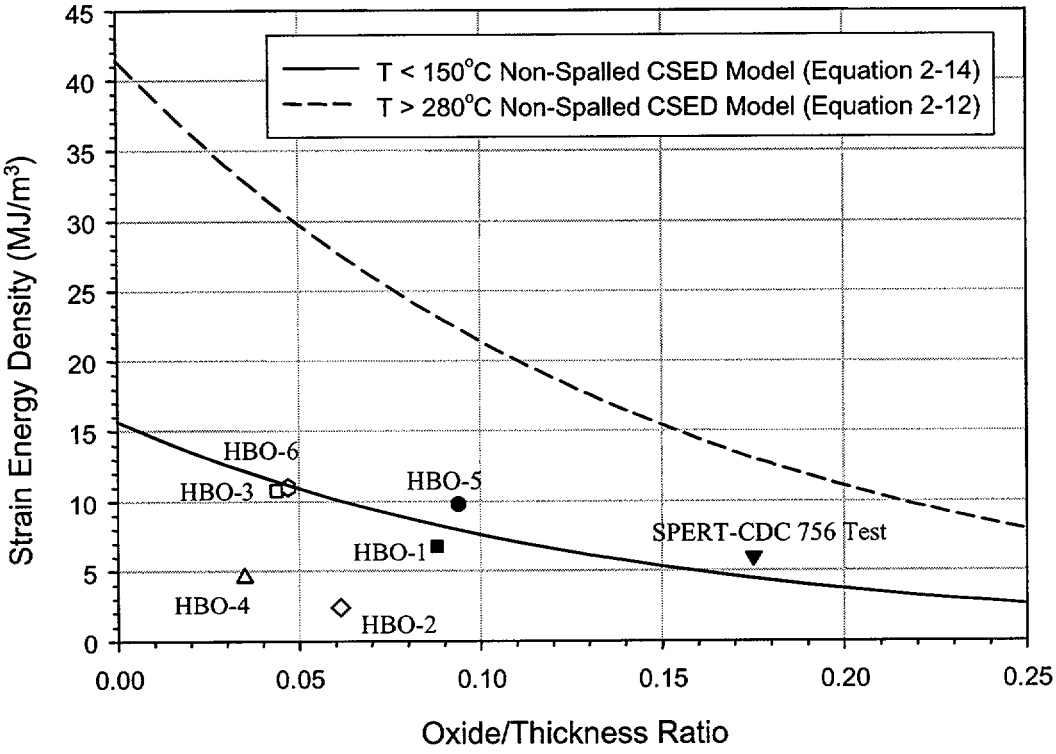

Figure 2-23
Strain Energy Density Results Calculated by FALCON for Selected NSRR Test Rods. The CSED models for non-spalled cladding at T < 150°C and T > 280°C are shown for comparison. It should be noted that part-wall cracks were observed in HBO-3 and HBO-6 in post-test examinations.

Two other methods to develop a cladding integrity model based on cladding strain limits have been evaluated using the FALCON analysis. As discussed in Section 2.3.2, failure curves based on a numerical fit of the total elongation data and uniform elongation data have been constructed from mechanical property tests performed at temperatures above 300°C. These failure curves were compared to the maximum cladding hoop strain calculated by FALCON for the CABRI REP Na tests summarized in Table 2-6. The results of the comparison are shown in Figure 2-24 for the total elongation limit and Figure 2-25 for the uniform elongation limit. For the total elongation curve, the maximum cladding hoop strains calculated by FALCON are below the curves for both unspalled and spalled cladding. Using the total elongation as a basis for developing a cladding integrity model does not separate between the non-failures and failures. In the case of the uniform elongation limit, REP Na-3 is predicted to fail using the non-spalled curve. Only REP Na-8 is predicted to fail using the spalled curve. REP Na-10 resides below the failure limit based on the uniform elongation for spalled cladding. The inability of using the either the total elongation or uniform elongation to predict cladding failure arises from two issues. First, the total elongation overestimates the capacity of the cladding to withstand the PCMI loading because of biaxiality effects. Even though the total elongation data have been corrected using a biaxiality correction factor, this correction factor is not consistent with the PCMI biaxial stress conditions calculated by FALCON. These differences diminish when the

mechanical property data are formulated in terms of critical strain energy density values. Second, the uniform elongation does not necessarily represent a failure limit for displacement control loading conditions, especially for material with some level of ductility. These results further support the coupled FALCON/SED approach for use in predicting cladding failure during the analysis of RIA-simulation experiments.

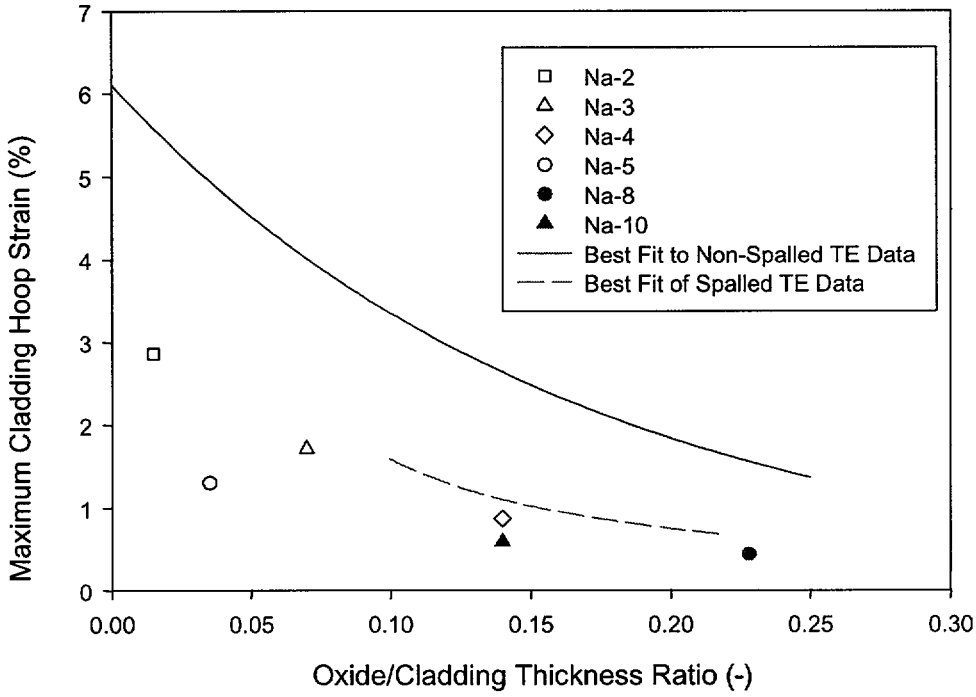

Figure 2-24
Maximum cladding hoop strain calculated by FALCON for the CABRI REP Na tests. Total elongation (TE) limit curves for spalled and non-spalled cladding are shown for comparison.

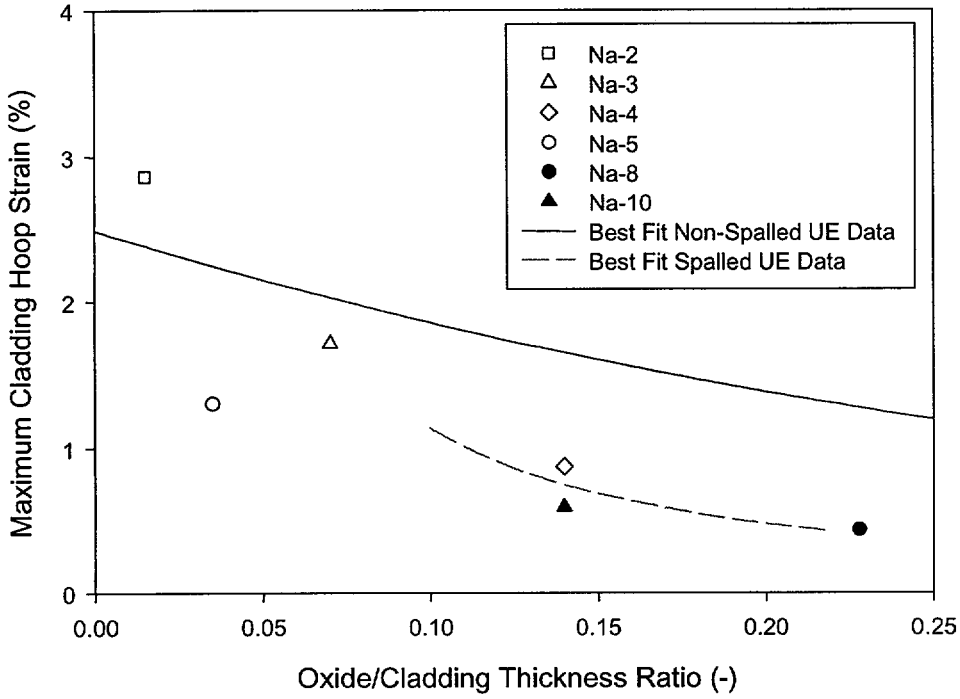

Figure 2-25
Maximum cladding hoop strain calculated by FALCON for the CABRI REP Na tests. Uniform elongation (UE) limit curves for spalled and non-spalled cladding are shown for comparison.

2.4.4 Summary

These results demonstrate the capability of FALCON to conservatively model the complex thermal and mechanical behavior of high burnup fuel during rapid energy depositions corresponding to a RIA event. As summarized in Table 2-6, the validation of FALCON for RIA analyses includes pulse widths between 4 milliseconds and 60 milliseconds, both 20°C and 300°C coolant temperature conditions, and different fuel rod types.

Analysis of the CABRI and NSRR tests find that an analytical translation is required to correct for the variation in the initial coolant temperature before a comparison of the fuel enthalpy levels is performed. The FALCON methodology provides for this translation through the calculation of the cladding SED response, and combined with CSED at the appropriate temperature condition, establishes a basis for a comparison. Furthermore, the analytical evaluation suggests that the CABRI tests performed in high temperature sodium represent well the PCMI phase of a postulated in-reactor RIA event and require only limited analysis to translate the results to PWR conditions. On the other hand, the NSRR tests conducted in room temperature stagnant water and under extremely narrow power pulses require analytical translation to PWR conditions before the results can be used to evaluate the fuel rod failure licensing bases.